

Constraining the primordial magnetic field with dwarf galaxy simulations

Mahsa Sanati¹, Yves Revaz¹, Jennifer Schober¹, Kerstin E. Kunze², Pascale Jablonka^{1,3}

¹ Institute of Physics, Laboratory of Astrophysics, École Polytechnique Fédérale de Lausanne (EPFL), 1290 Sauverny, Switzerland
e-mail: mahsa.sanati@epfl.ch

² Departamento de Física Fundamental, Universidad de Salamanca, Plaza de la Merced s/n, 37008 Salamanca, Spain

³ GEPI, CNRS UMR 8111, Observatoire de Paris, PSL University, 92125 Meudon, Cedex, France

Received: XXXX; accepted: YYYY

ABSTRACT

Using a set of cosmological hydro-dynamical simulations, we constrained the properties of primordial magnetic fields by studying their impact on the formation and evolution of dwarf galaxies. We performed a large set of simulations (8 dark matter only and 72 chemo-hydrodynamical) including primordial magnetic fields through the extra density fluctuations they induce at small length scales ($k \geq 10 h \text{Mpc}^{-1}$) in the matter power spectrum. Our sample of dwarfs include 9 systems selected out of the initial $(3.4 \text{Mpc}/h)^3$ parent box, re-simulated from $z = 200$ to $z = 0$ using a zoom-in technique and including the physics of baryons. We explored a large variety of primordial magnetic fields with strength B_λ ranging from 0.05 to 0.50 nG and magnetic energy spectrum slopes n_B from -2.9 to -2.1 . Strong magnetic fields characterized by a high amplitude ($B_\lambda = 0.50, 0.20 \text{ nG}$ with $n_B = -2.9$) or by a steep initial power spectrum slope ($n_B = -2.1, -2.4$, with $B_\lambda = 0.05 \text{ nG}$) induce perturbations in the mass scales from 10^7 to $10^9 M_\odot$. In this context emerging galaxies see their star formation rate strongly boosted. They become more luminous and metal rich than their counterparts without primordial magnetic fields. Such strong fields are ruled out by their inability to reproduce the observed scaling relations of dwarf galaxies. They predict dwarf galaxies to be at the origin of an unrealistically early reionization of the Universe and also overproduce luminous satellites in the Local Group. Weaker magnetic fields impacting the primordial density field at corresponding masses $\lesssim 10^6 M_\odot$, produce a large number of mini dark halos orbiting the dwarfs, however out of reach for current lensing observations. This study allows for the first time to constrain the properties of primordial magnetic fields based on realistic cosmological simulations of dwarf galaxies.

Key words. primordial magnetic fields, cosmology, dwarf galaxy, galaxy evolution

1. Introduction

Magnetic fields have been observed on all cosmic scales probed so far, from planets and stars (Stevenson 2010; Reiners 2012) to galaxies (Beck 2001; Beck & Wielebinski 2013) and galaxy clusters (Clarke et al. 2001; Govoni & Feretti 2004; Vogt & Enßlin 2005). There are numerous observational evidences for magnetic fields with a strength of a few to tens of micro Gauss coherent on scales up to ten kpc, detected through radio spectropolarimetry in spiral galaxies like M51 (Fletcher et al. 2011; Beck 2015), and ultra luminous infrared galaxies (ULIRGs) (Robishaw et al. 2008; McBride & Heiles 2013), but also in high redshift galaxies (Bernet et al. 2008; Mao et al. 2017) and in the interstellar and intergalactic medium (Han 2017). However, understanding the origin and strength of the fields is still a challenge for modern astrophysics.

There are various theories proposed to explain the generation of magnetic fields on large scales and their amplification by a dynamo in collapsed objects (Ichiki & Takahashi 2006; Ryu et al. 2008; Naoz & Narayan 2013; Schober et al. 2013), or the generation of magnetic fields on small scales (Widrow 2002; Hanayama et al. 2005; Safarzadeh 2018). However, recent observational evidences based on blazar emissions suggest that intergalactic medium voids could host a weak $\sim 10^{-16}$ Gauss magnetic field, coherent on Mpc scales (Neronov & Vovk 2010; Kandus et al. 2011). Such a field is difficult to be purely explained by turbu-

lence in the late universe (Furlanetto & Loeb 2001; Bertone et al. 2006) and would perhaps favor a primordial origin in the early universe (Subramanian 2016; Kahniashvili et al. 2020; Jedamzik & Pogosian 2020).

Recently new observational signatures of primordial magnetic fields have been obtained from the Lyman- α forest clouds (Pandey & Sethi 2013), the two-point shear correlation function from gravitational lensing (Pandey & Sethi 2012), the Sunyaev-Zel'dovich statistics (Tashiro et al. 2009), the cosmic microwave background (CMB) anisotropies (Shaw & Lewis 2010; Planck Collaboration et al. 2015; Zucca et al. 2017; Paoletti et al. 2019), CMB spectral distortions (Jedamzik et al. 2000; Kunze & Komatsu 2014; Wågstaff & Banerjee 2015) large scale structure (Kahniashvili et al. 2010) and the reionization history of the Universe (Pandey et al. 2015).

The above observations provide new upper limits on the strength of the fields which appeared to be limited to 47 pG for scale-invariant fields (Jedamzik & Saveliev 2019) and a few nG in more general states coherent on 1 Mpc. It is thus of great interest to ask if such primordial fields can be confirmed and how their characteristics can be constrained further.

To answer this issue we need to journey back to the early universe. The present day large scale structures are thought to be seeded by quantum field fluctuations when the relevant scales were causally connected, leading to a nearly scale-invariant fluctuation spectrum (Dodelson 2003; Kolb & Turner 1990; Pad-

manabhan 2002). These scales then crossed the universe horizon during the inflationary expansion phase, and re-enter only later to serve as the initial conditions, leading to the growth of large scale structures. It is likely that the origin of the magnetic fields also arises during various phase transitions in the early universe (Turner & Widrow 1988a; Adshedd et al. 2016; Domcke et al. 2019; Fujita & Durrer 2019) by a small fraction of the energy released during the electroweak or quark-hadron transitions and converted to large scale magnetic fields (Hogan 1983; Ratra 1992a).

A primordial magnetic field (PMF) in the post-recombination epoch generates density fluctuations in addition to the standard inflationary fluctuations. The magnetically-induced perturbations, for a scale-invariant magnetic spectrum, may dominate the standard Λ CDM matter power spectrum on small length scales and therefore can affect the formation of the first galaxies (Kim et al. 1996; Wasserman 1978b). Indeed, the Λ CDM paradigm implies a hierarchical formation of galaxies, in which dwarf galaxies, including the ultra-faint ones (UFDs) (Simon 2019) as observed today are the best analogs to the smallest initial building blocks. A modification of the nearly power-law spectrum of the Λ CDM model at small scales ($k \geq 10 h \text{Mpc}^{-1}$) will thus directly affect the number and properties of dwarf galaxies with interesting outcomes for understanding the cosmological model and origin of the magnetic field.

Changing the abundance of dwarf galaxies and their structure can potentially shed new light on the long standing tensions existing between dark matter only (DMO) Λ CDM cosmological simulations and Local Group observations (see Bullock & Boylan-Kolchin (2017) for a recent review). Among the existing tensions, the over-prediction of small mass systems around the Milky Way, the so-called missing satellite problem (Klypin et al. 1999; Moore et al. 1999) and the too big to fail problem (Boylan-Kolchin et al. 2011, 2012) are certainly the most emblematic ones. Along with the number of observed satellites, their mass profile is also known to suffer from tensions. DMO simulations predict the dark halos to follow an universal cuspy profile (Navarro et al. 1996, 1997), while observations favour cored ones (Moore (1994); Flores & Primack (1994), see Read et al. (2018) for a short review.) While improvements in the baryonic treatment of cosmological simulations allowed for a reduction of those tensions (Chan et al. 2015; Sawala et al. 2016; Wetzel et al. 2016; Verbeke et al. 2017; Revaz & Jablonka 2018; Pontzen & Governato 2014; Oñorbe et al. 2015; Chan et al. 2015; Fitts et al. 2017; Hausammann et al. 2019), modification or alternative to the Λ CDM have been proposed too, like warm dark matter (Lovell et al. 2012; Governato et al. 2015; Fitts et al. 2019), self-interacting dark matter (Vogelsberger et al. 2014; Harvey et al. 2018; Fitts et al. 2019) or wave dark matter (Chan et al. 2018).

On the other hand, the plethora of observations available for dwarf galaxies in the Local Group may be used to constrain the amplitude of PMFs. Any model including the effect of PMFs must reproduce i) the abundances of detected satellites around the Milky Way (Newton et al. 2018; Nadler et al. 2018; Drlica-Wagner et al. 2019), ii) the well known observed scaling relations (Mateo 1998; Tolstoy et al. 2009; McConnachie 2012; Simon 2019), as well as more detailed properties like line-of-sight (LOS) velocity dispersion, stellar abundance patterns and star formation histories (Tolstoy et al. 2009), and iii) they must be in agreement with the Milky Way local reionization history. Indeed, by hosting the first generation of stars and lightening up the dark ages (Choudhury et al. 2008; Salvadori et al. 2014; Wise et al. 2014; Robertson et al. 2015; Bouwens et al. 2015; Atek

et al. 2015), dwarf galaxies played a key role during the epoch of reionization.

The above arguments make dwarf and UFD galaxies excellent laboratories to study the subtle impact of initial conditions imposed after the inflation and how they rule the first structures. As such, they may be used to get new constraints on the properties of PMFs (Safarzadeh & Loeb 2019).

Recently Revaz & Jablonka (2018) demonstrated that cosmological simulations run with the code GEAR reproduce a wide range of observed properties of the Local Group dwarf galaxies. Relying on this previous work, we take the opportunity to study for the first time, the formation and evolution of a suite of dwarf galaxies that emerge from a Λ CDM cosmology where the primordial density fluctuations include the effect of PMFs. Our goal is to size the impact of these primordial fields on the properties of dwarf galaxies.

This paper is organized as follows: Section 2, recalls the theory around PMFs and their effect on the density fluctuation power spectrum. Section 3, describes in details our numerical framework as well as the simulations performed. The results are presented in Section 4. We first discuss results relying on dark matter only simulations and show how the PMFs affect the matter halo mass function at small scales. In a second part, we focus on zoom-in hydro-dynamical simulations. We study the impact of PMFs on the properties of dwarf galaxies and in particular on scaling relations. We then estimate how the modified properties of dwarfs directly impact the reionization history of the Universe as well as the cumulative number of bright satellites around the Milky Way. Limits on the properties of PMFs are obtained by comparing with existing observational constraints. A brief conclusion is given in Section 5.

2. Impact of Primordial Magnetic Fields on the density fluctuations

We consider the effect of PMFs generated before recombination by processes occurring during the inflationary epoch (ex. Turner & Widrow 1988b; Ratra 1992b). It has been shown in the seminal works of Wasserman (1978a) and Kim et al. (1996) that after the recombination epoch, PMFs may induce motions in the ionized baryons through the Lorentz force which drives compressional and rotational perturbations causing density fluctuations in the gas. Those perturbations propagate down to other non-ionized components, the neutral gas but also the dark matter are coupling through the gravitational force and a direct impact on the total matter power spectrum is expected.

Characterizing this impact is however non-trivial and a large literature has been dedicated to describe it. Hereafter, without entering into too much detail, we briefly review the principal steps that allow to catch the origin of the effect of primordial magnetic fields on the total matter power spectrum.

2.1. The primordial magnetic field

Following Wasserman (1978a); Kim et al. (1996); Gopal & Sethi (2003), we first assume that the tangled magnetic field results from a statistically homogeneous and isotropic vector random process. The two-point correlation function of a non-helical field in Fourier space can then be expressed as:

$$\langle \hat{B}_i(\mathbf{k}) \hat{B}_j^*(\mathbf{k}') \rangle = (2\pi)^3 \delta(\mathbf{k} - \mathbf{k}') \frac{P_{ij}(\mathbf{k}, \mathbf{k}')}{2} P_B(k), \quad (1)$$

where $P_{ij}(\mathbf{k}) = \delta_{ij} - \frac{k_i k_j}{k^2}$, $k = |\mathbf{k}|$ is the comoving wave number and $P_B(k)$ is the magnetic field power spectrum. Without further information on the exact origin of the PMFs, it is usually assumed that its power spectrum follows a simple power law:

$$P_B(k) = A k^{n_B} \quad (2)$$

where n_B is the slope index, and A the amplitude of the magnetic spectrum, which is defined through the variance of the magnetic field strength B_λ^2 at a scale $\lambda = 1 \text{ Mpc} \equiv k_\lambda^{-1}$, namely (Shaw & Lewis 2012):

$$A = \frac{(2\pi)^{n_B+5} B_\lambda^2}{2\Gamma(\frac{n_B+3}{2}) k_\lambda^{n_B+3}}. \quad (3)$$

With those definitions, n_B and B_λ fully characterise the PMFs. They constitute our main free parameters.

2.2. Growth of perturbations

In the linearized Newtonian theory, the evolution of density fluctuations in the presence of PMFs is described by the two following coupled equations, respectively, for the baryonic fluid perturbation field $\delta_b(\mathbf{x}, t) = \delta\rho_b(\mathbf{x}, t)/\bar{\rho}_b$ and for the collisionless dark matter $\delta_{\text{DM}}(\mathbf{x}, t) = \delta\rho_{\text{DM}}(\mathbf{x}, t)/\bar{\rho}_{\text{DM}}$ (see for example Subramanian & Barrow 1998; Sethi & Subramanian 2005):

$$\frac{\partial^2}{\partial t^2} \delta_b + \left[2H + \frac{4\rho_\gamma}{3\rho_b} n_e \sigma_T a \right] \frac{\partial}{\partial t} \delta_b = c_b^2 \nabla^2 \delta_b + 4\pi G a^2 [\rho_b \delta_b + \rho_{\text{DM}} \delta_{\text{DM}}] + \frac{S(\mathbf{x}, t)}{a^3}, \quad (4)$$

and

$$\frac{\partial^2}{\partial t^2} \delta_{\text{DM}} + 2H \frac{\partial}{\partial t} \delta_{\text{DM}} = 4\pi G a^2 [\rho_b \delta_b + \rho_{\text{DM}} \delta_{\text{DM}}]. \quad (5)$$

Here, a is the scale factor, $H = \dot{a}/a$ the Hubble constant, ρ_b and ρ_γ the baryon and photon mass density, n_e the electron number density, σ_T the Thomson cross-section for electron-photon scattering, and c_b the baryon sound speed. S represents the magnetic field source term normalized to the baryon density at the present time, $\bar{\rho}_b(t_0)$:

$$S(\mathbf{x}, t) = \frac{\nabla \cdot [\mathbf{B} \times (\nabla \times \mathbf{B})]}{4\pi \bar{\rho}_b(t_0)}, \quad (6)$$

The baryon pressure term $c_b^2 \nabla^2 \delta_b$ in Eq. 4 is sub-dominant with respect to the magnetic pressure as long as the background magnetic field is larger than $5 \times 10^{-11} \text{ G}$ (Subramanian & Barrow 1998) and may thus be ignored. The damping term involving the Thomson cross-section corresponds to the radiation viscosity. Prior to recombination, this term leads to the damping of small scale magnetic waves (Jedamzik et al. 1998; Subramanian & Barrow 1998), a physical process similar to the Silk damping (Silk 1968). This induces a sharp cutoff of the magnetic field when entering the recombination epoch and subsequently, to its contribution in the total matter power spectrum.

Introducing the total matter density perturbation:

$$\delta_m(\mathbf{x}, t) = (\bar{\rho}_{\text{DM}} \delta_{\text{DM}} + \bar{\rho}_b \delta_b) / \bar{\rho}_{\text{DM}}, \quad (7)$$

we can solve Eqs. 4 and 5 and get the time evolution of δ_m only due to the magnetic fields (Sethi & Subramanian 2005):

$$\delta_m \sim \frac{3}{5} \frac{\Omega_b}{\Omega_m^2} \left[\frac{3}{2} \left(\frac{t}{t_{\text{rec}}} \right)^{2/3} + \left(\frac{t_{\text{rec}}}{t} \right) - \frac{5}{2} \right] S(\mathbf{x}, t_{\text{rec}}) t_{\text{rec}}^2, \quad (8)$$

where t_{rec} is the time at recombination and Ω_m and Ω_b are the matter and baryon density parameters.

The important point to get from the previous equations is that the spatial dependence of $\delta_m(\mathbf{x}, t)$ can be followed through the magnetic field source term $S(\mathbf{x}, t_{\text{rec}})$. We thus expect the total matter power spectrum to directly depend on the power spectrum of the magnetic field.

It is worth noting that the most significant evolution of the magnetic field takes place before recombination (Kahniashvili et al. 2013; Brandenburg et al. 2017a,b). During recombination the ionization degree drops to a tiny value. Afterwards the magnetic field is more or less frozen into the gas, i.e., it just follows passively the cosmic expansion, ensuring the magnetic flux to be conserved.

2.3. Impact on the total matter power spectrum

The modification of the total matter power spectrum due to the influence of magnetic fields has been first addressed by Kim et al. (1996) and extended by Gopal & Sethi (2003). The total matter power spectrum is the ensemble average of the density fluctuations in the Fourier space, $P(k, t) = \langle \delta_m(k, t) \delta_m^*(k, t) \rangle$, that we can obtain from the evolution equation (Eq. 7) and introducing the ensemble average of the PMFs, Eq. 6 and 2.

After the decoupling of photons, the ionized matter density fluctuations are affected by the magnetic Alfvén waves if the crossing time, $\tau_A \sim 1/k v_A$, is smaller than the inverse Hubble rate (Banerjee & Jedamzik 2004), where v_A is the Alfvén velocity $v_A = B_\lambda / \sqrt{\mu_0 \rho_0}$, with μ_0 the permeability or magnetic constant. As the magnetic energy B_λ^2 scales with $P_B(k) k^3$, $\tau_A \sim \sqrt{\mu_0 \rho_0} k^{-(3+n_B)/2}$. For $n_B > -5$, the crossing time is then shorter for larger k , amplifying the perturbations faster at smaller scales. In the limit where $k \ll k_B$, with $k_B \equiv (v_A \sqrt{\pi/\rho_0 G})^{-1}$, the magnetic wave number above it the Alfvén waves damp instabilities (the equivalent of the Jeans wave number), at lowest order in k/k_{max} , i.e., $k_{\text{max}} \equiv k_B$, the solution for the total matter power spectrum is (Gopal & Sethi 2003):

$$P(k) \sim A k^{2n_B+7} + B k_{\text{max}}^{2n_B+3} k^4 + C k_{\text{max}}^{2n_B+1} k^6 + \dots \quad (9)$$

which strongly depends on the magnetic slope index n_B . For the scale-invariant case, $n_B \cong -3$, $P(k) \sim k$, and $\tau_A \sim k^{-1}$, thus small scale perturbations are strongly amplified, as long as $\tau_A < 1/H(t)$, up to about k_B where they are sharply quenched (see 2.2).

2.4. The adopted total matter power spectrum

We generated the matter power spectrum using a modified version of the CAMB code which includes the effects of PMFs (for details see Shaw & Lewis (2012)). In this version, the non-linear effects of both the magnetic Jeans length (magnetic pressure) and the damping due to the radiation viscosity (when the photon free streaming length is small) is explicitly computed. As such, contrary to other studies, there is no need to artificially include a cutoff wave number.

Figures 1 and 2 display the matter power spectrum due to the magnetic field (dashed lines) together with its contribution to the total matter power spectrum (plain lines). The black continuous line corresponds to the unperturbed Λ CDM power spectrum. The dependence with respect to the magnetic field amplitude ($B_\lambda = 0.05, 0.10, 0.20, 0.50 \text{ nG}$) is shown in Figure 1 keeping the spectral index constant ($n_B = -2.9$). The dependence with respect to the spectral index with $B_\lambda = 0.05 \text{ nG}$ is shown

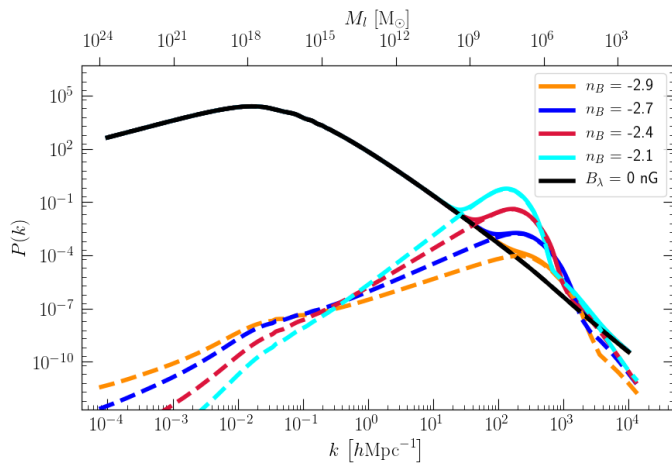


Fig. 1: The contribution of the magnetically induced power spectrum for a variety of magnetic field indexes (dashed colored lines) to the total matter power spectrum (plain colored lines). The unperturbed Λ CDM spectrum is shown in the black continuous line. The magnetic field strength is kept constant at $B_\lambda = 0.05$ nG.

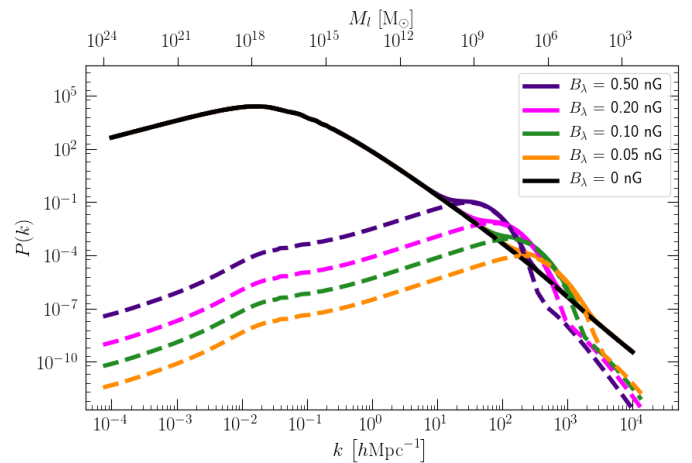


Fig. 2: The contribution of the magnetically induced power spectrum to the total matter power spectrum. Same figure as Fig. 1 with constant spectral slope, $n_B = -2.9$, and varying magnetic field amplitudes.

on Fig. 2. The range of parameters explored is chosen in such a way that they impact the power spectrum without violating the existing constraints as the ones presented in Section 1.

It is worth mentioning that, for the magnetic spectral index, a range of both positive and negative values are suggested. In this study, we considered PMFs generated during the inflation, which tend to have negative values for n_B , (Turner & Widrow 1988a; Ratra 1992a; Giovannini & Shaposhnikov 2000; Martin & Yokoyama 2008). However, positive values for n_B are also plausible in other magnetogenesis processes, like the electroweak phase transition (Grasso & Rubinstein 2001; Kandus et al. 2011; Durrer & Neronov 2013), Higgs field gradients (Vachaspati 1991), or in the case of subsequent evolution of the PMFs, e.g. via the chiral anomaly (Boyarsky et al. 2012; Rogachevskii et al. 2017; Schober et al. 2018).

As expected from Eq. 9, at large scales (small k), for $n_B = -2.9$ the slope is nearly 1 and increases for increasing n_B . Small scale structures are thus strongly magnetically amplified and reach an amplitude larger than the one induced by inflation only. At very small scales, the power spectrum is sharply quenched owing to the magnetic pressure and radiation viscosity damping. The total power spectrum is thus characterised by a bump at the smallest amplified scales, $k \sim 10 - 1000$ $h\text{Mpc}^{-1}$ depending on the exact values of n_B and B_λ . In Fig. 1 and 2 we link the wave number and the mass contained within a sphere of comoving Lagrangian radius r_l at $z = 0$ by defining the mass scale M_l (the equivalent of the Jeans mass), assuming a background mean density given by the cosmological parameters (see for example Bullock & Boylan-Kolchin 2017):

$$M_l = \frac{4\pi}{3} r_l^3 \rho_m = \frac{\Omega_m H_0^2}{2G} r_l^3 = 1.71 \times 10^{11} M_\odot \left(\frac{\Omega_m}{0.3}\right) \left(\frac{h}{0.67}\right)^2 \left(\frac{r_l}{1\text{Mpc}}\right)^3 \quad (10)$$

The bumps precisely cover masses expected for the total mass of dwarf galaxies. Therefore, PMFs could significantly influence the formation and properties of those objects.

From Fig. 1 and 2, it appears that a steeper slope or a stronger amplitude would affect the power spectrum for $k < 10$ $h\text{Mpc}^{-1}$.

Such a modification is ruled out by the observations of the Lyman- α forest (Tegmark & Zaldarriaga 2002; Pandey & Sethi 2013).

3. Simulations

We performed a set of Λ CDM cosmological simulations with initial conditions that match the perturbed range of the total matter power spectrum described above. We used the same $(3.4 \text{ Mpc}/h)^3$ box adopted by Revaz & Jablonka (2018) to study dwarf galaxies. The cosmology is the one described by the Planck Collaboration et al. (2016b) with: $\Omega_\Lambda = 0.685$, $\Omega_m = 0.315$, $\Omega_b = 0.0486$, $H_0 = 67.3 \text{ km s}^{-1} \text{ Mpc}^{-1}$, $n_s = 0.9603$, $\sigma_8 = 0.829$.

Two types of simulations have been realized: (i) Dark Matter Only (DMO) simulations of the entire box, used to compute the halo mass function and its dependency on the PMFs (ii) hydro-dynamical simulations of a selection of dwarf galaxies with the zoom-in technique. They allow to check the effect of PMFs on the properties of stellar populations.

3.1. Initial conditions

The initial conditions have been generated using the code MUSIC (Hahn & Abel 2011). Instead of using, the Eisenstein & Hu (1998), the default MUSIC power spectrum, we designed a special plug-in to use the total matter power spectrum obtained from the modified CAMB code. Compared to the Eisenstein & Hu function, the latter includes baryonic pressure which leads to additional power at scales larger than $k \cong 100$ $h\text{Mpc}^{-1}$, and results in almost a 10 % difference in the mass content of structures formed in models without a magnetic fields.

For the DMO simulations we used the resolution of level 9. This corresponds to $(2^9)^3$ particles, covering the entire box. For the hydro-dynamical simulations we used the zoom-in technique to gradually degrade the resolution from level 9 to level 6 outside the refined regions. With this setting, the mass resolution of dark matter, gas and stellar particles is $22'462 h^{-1} M_\odot$, $4'096 h^{-1} M_\odot$ and $1'024 h^{-1} M_\odot$, respectively.

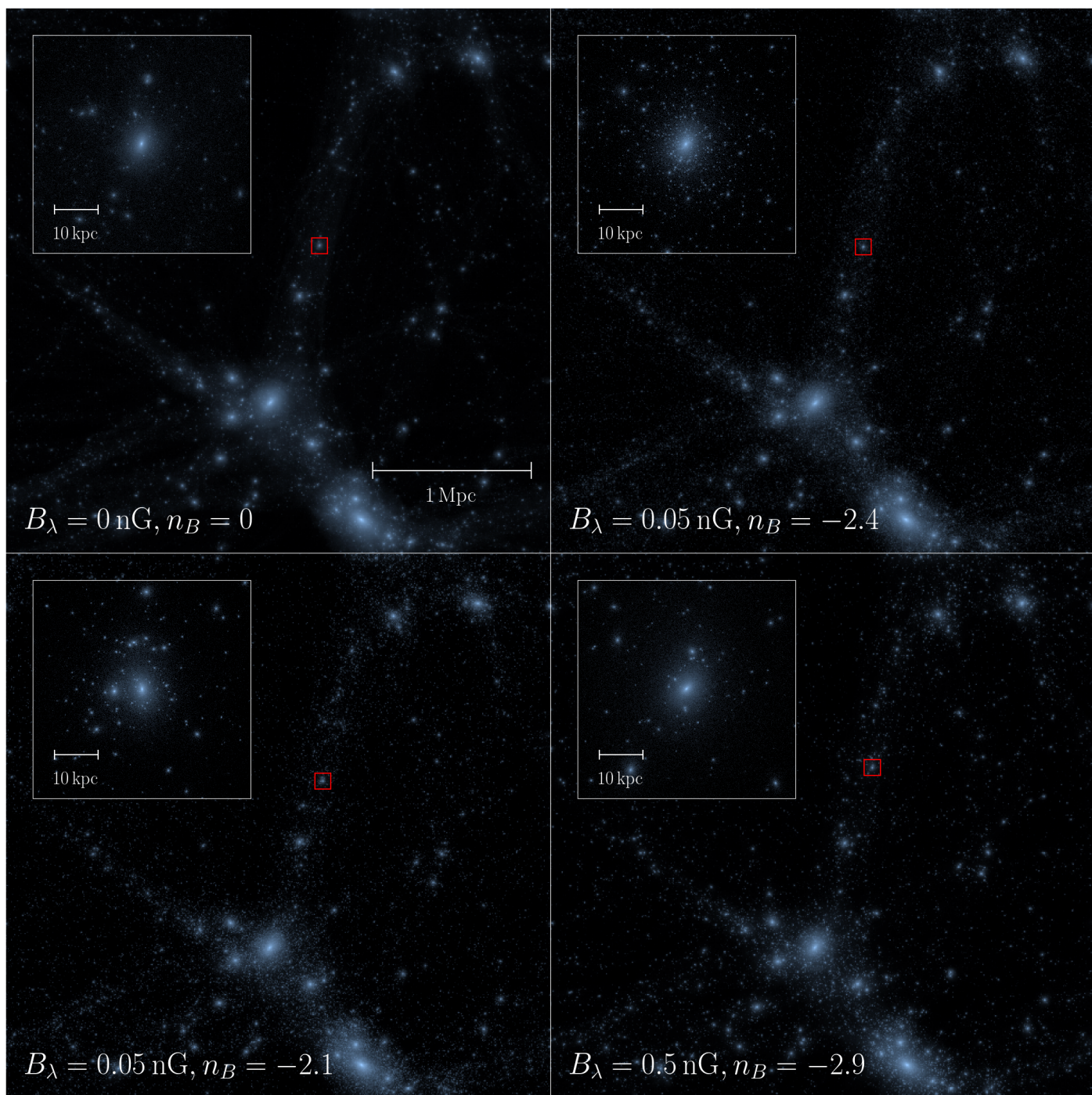


Fig. 3: Surface density projections of three DMO simulations at $z = 0$ with different PMFs as indicated on the bottom. In all plots, the upper square is a zoom on a dwarf indicated by the red central squares.

3.2. Code evolution

The simulations have been run with the chemo-dynamical Tree/SPH code GEAR developed by Revaz & Jablonka (2012), Revaz et al. (2016) and Revaz & Jablonka (2018). GEAR is a fully parallel code based on Gadget-2 (Springel 2005). It operates with individual and adaptive time steps (Durier & Dalla Vecchia 2012) and includes recent SPH improvements such as the pressure-entropy formulation (Hopkins 2013). GEAR includes radiative gas cooling and redshift-dependent UV-background heating through the GRACKLE library (Smith et al. 2017). The metal line cooling is computed through the Cloudy code (Ferland et al.

2013) for solar abundances which is scaled according to the gas metallicity. Hydrogen self-shielding against the ionizing radiation is incorporated by suppressing the UV-background heating for gas densities above $n_H = 0.007 \text{ cm}^{-3}$ (Aubert & Teyssier 2010). Star formation relies on the stochastic prescription proposed by Katz (1992); Katz et al. (1996). We used an efficiency of star formation parameter $c_* = 0.01$. The star formation recipe is supplemented by a modified version of the Jeans pressure floor (Hopkins et al. 2011; Revaz & Jablonka 2018) by adding a non-thermal term in the equation of state of the gas to avoid any spurious gas fragmentation. The chemical evolution includes Type Ia and II supernovae (SNe) with yields taken from Tsujimoto et al.

Table 1: The combination of explored parameters B_λ and n_B used for the seven simulations performed with a magnetically perturbed power spectrum. The models are referred in the paper as the model names given below.

model	B0.05n2.9	B0.05n2.7	B0.05n2.4	B0.05n2.1	B0.10n2.9	B0.20n2.9	B0.50n2.9
B_λ [nG]	0.05	0.05	0.05	0.05	0.10	0.20	0.50
n_B	-2.9	-2.7	-2.4	-2.1	-2.9	-2.9	-2.9

(1995) and Kobayashi et al. (2000), respectively. GEAR includes thermal blastwave-like feedback, for which 10% of the explosion energy of each SN, taken as 10^{51} erg, is released in the interstellar medium (i.e., the SN efficiency is $\epsilon = 0.1$). The initial mass function (IMF) is sampled with the random discrete scheme (RIMFS) of Revaz et al. (2016). The released chemical elements are mixed using the Smooth Metallicity Scheme (Okamoto et al. 2005; Tornatore et al. 2007; Wiersma et al. 2009).

3.3. The set of simulations

Each type of simulations, DMO and zoom-in, have been run eight times. A first run is performed without magnetically-induced perturbations and seven others explore the effect of B_λ and n_B parameters with values given in Tab. 1 and corresponding to the total matter power spectra of Fig. 1 and 2.

We selected nine halos from the 27 dwarfs presented in Revaz & Jablonka (2018) and re-simulated them with the same zoom-in technique. The selection covers galaxies with $L_V < 10^7 L_\odot$, where L_V stands for the total V-band luminosity, and different star formation histories. Seven dwarfs are dominated by an old stellar population, being quenched by the UV-background after at most four billion years and two dwarfs are more massive, characterized by extended star formation histories. The list of the re-simulated dwarf galaxies is given in Tab. 3 with their basic properties as obtained in the unperturbed case at $z = 0$: total V-band luminosity L_V , total stellar mass M_\star and virial mass M_{200} , where the virial overdensity is 200 times the critical density.

All simulations have been started at a redshift of 200, ensuring that the rms variance of the initial density field, σ_8 , lies between 0.1 and 0.2 (Knebe et al. 2009). At the exception of the extreme cases, all halos reached $z = 0$ (the reason of the crash will be discussed later on).

4. Results

4.1. DMO simulations and halo mass function

Figure 3 displays the dark matter surface density at $z = 0$ of four models: the unperturbed Λ CDM model and three models with the magnetically induced bumps in the power spectrum that peak at different mass scales: B0.05n2.4 ($M_{\text{peak}} \cong 5 \cdot 10^6 M_\odot$), B0.05n2.1 ($M_{\text{peak}} \cong 3 \cdot 10^7 M_\odot$), and B0.50n2.9 ($M_{\text{peak}} \cong 2 \cdot 10^8 M_\odot$). As expected, the small scale bump increases the number of sub-dark halos orbiting around dwarf galaxies. This number decreases with increasing the mass of the halos. To quantify the effect of the bump observed in the total matter power spectrum, for all our DMO simulations, we investigate the abun-

Table 3: The list of the 9 dwarf galaxies simulated with the zoom-in technique. For each of them, we provide the total V-band luminosity L_V , total stellar mass M_\star and virial mass M_{200} and the star formation type, for the unperturbed models at $z = 0$.

model ID	L_V [$10^6 L_\odot$]	M_\star [$10^6 M_\odot$]	M_{200} [$10^9 M_\odot$]	SF Class
h050	4.2	9.6	2.6	Extended
h070	2.0	5.8	1.8	Extended
h061	0.2	0.5	1.9	Quenched
h141	0.2	0.6	0.8	Quenched
h111	0.2	0.5	1.1	Quenched
h122	0.1	0.4	1.0	Quenched
h159	0.4	1.1	0.7	Quenched
h168	0.1	0.3	0.6	Quenched
h177	0.2	0.5	0.5	Quenched

dance of dark matter sub-halos. We extracted dark halos using the Rockstar halo finder (Behroozi et al. 2013) that uses an adaptive hierarchical refinement of the friends-of-friends algorithm. All extracted halos consist of particle groups that are overdense with respect to the local background and contain a minimum of 100 bounded particles.

Fig. 4 and 5 show the halo mass function, i.e., the number of dark matter halos, dN , per unit mass interval, dM . All mass functions are truncated below $3 \cdot 10^5 M_\odot$, which corresponds to the limit of our mass resolution. While halos are detected with masses up to about $5 \cdot 10^{10} M_\odot$, the relatively small size of the box prevents to generate many of those. This makes the curve noisy and we truncated it above $2 \cdot 10^9 M_\odot$. Between these limits, the unperturbed power spectrum is nicely fitted by a power-law,

$$\frac{dN}{dM} = a_0 \left(\frac{M}{m_0} \right)^\alpha, \quad (11)$$

with an amplitude of $a_0 = 8.79 \times 10^7 / M_{\text{vir}} = 4.46 \times 10^{-5} M_\odot^{-1}$, a pivot point of $m_0 = 10^{-5} M_{\text{vir}} = 1.97 \times 10^7 M_\odot$ and a slope of $\alpha = -1.96$. Those parameters perfectly match previous studies (see for example Springel et al. 2008). The fit to the halo mass function is shown in dashed gray line.

The bottom panels of Fig. 4 and 5 show the ratio between the magnetically modified halo mass function and the unperturbed one. Depending on the strength and the spectral index of the magnetic field, each PMF model affects the halo mass function in a different mass range below $\sim 10^9 M_\odot$, reflecting the corresponding mass of the bump in the power spectrum. For a fixed magnetic amplitude, increasing the slope from $n_B = -2.7$

Table 2: Values of the fitting parameters used in Eq. 12 for different PMF models.

model	B0.05n2.9	B0.05n2.7	B0.05n2.4	B0.05n2.1	B0.10n2.9	B0.20n2.9	B0.50n2.9
c	3.00	6.71	7.79	7.35	4.50	4.06	3.86
u	5.30	6.14	7.07	7.85	6.17	7.08	8.45
s	0.80	0.60	0.57	0.52	0.70	0.70	0.67

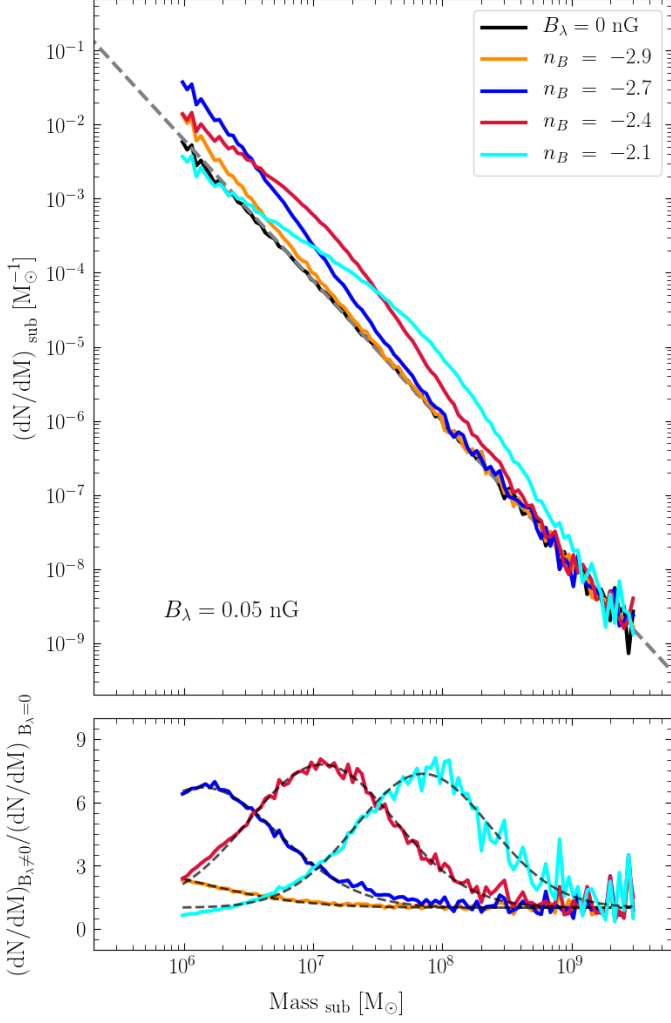


Fig. 4: Halo mass function. The halo mass is calculated within R_{200} . We show the count of subhalos per logarithmic mass interval for different slope indexes n_B with a constant magnetic field strength, $B_\lambda = 0.05$ nG. The dashed gray line shows a power-law $dN/dM \sim M^{-1.96}$ fitted the unperturbed power spectrum. The bottom panel shows the ratio between the halo mass function of each PMF model and the unperturbed model. The dashed lines correspond to the fit given by Eq. 12.

to -2.1 , shifts the bump from about $10^6 M_\odot$ to $5 \cdot 10^7 M_\odot$. In average, in a one dex mass range around the maximum of the bump, between 5 to 7 times more halos are present compared to the generic model without magnetic fields. Similarly, when the slope is fixed, increasing the magnetic amplitude, B_λ , shifts the bump upwards, increasing their number by a factor between 3 and 4.

We found the ratio between the perturbed and unperturbed halo mass functions to be well fitted by a simple modified Gaussian function:

$$\left(\frac{dN}{dM}\right) / \left(\frac{dN}{dM}\right)_{\text{unperturbed}} = (c - 1) \exp\left[-\frac{(\log_{10}(M) - u)^2}{2s^2}\right] + 1 \quad (12)$$

with values for c , u and s given in Tab. 2. The fit is shown by a dashed line on the bottom panel of Fig. 4 and 5. Equation 12 is convenient to estimate analytically the magnetically perturbed

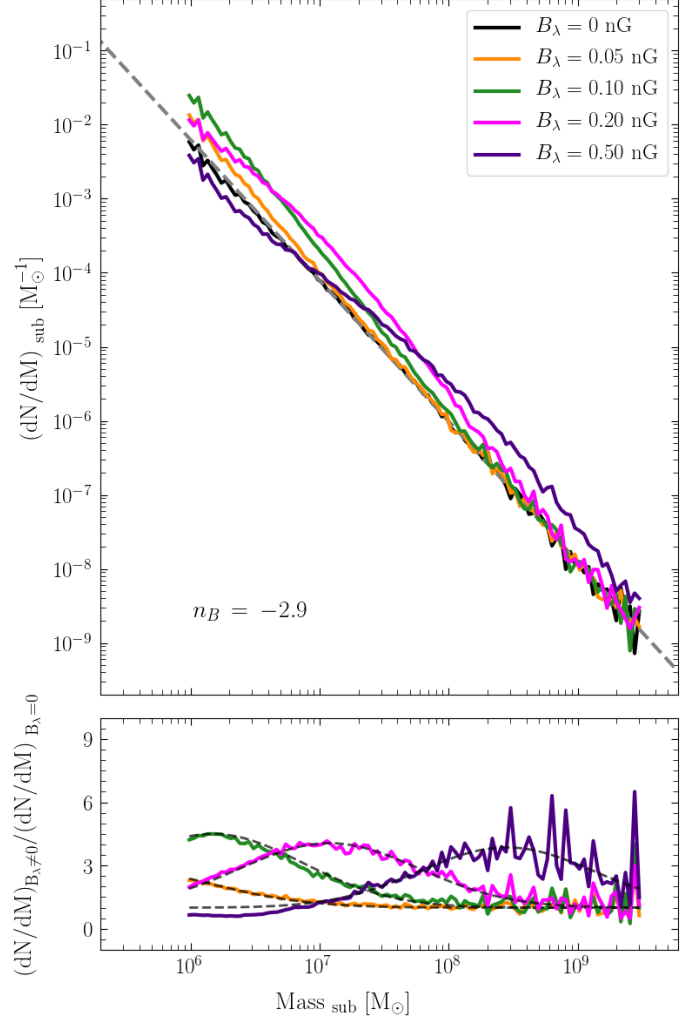


Fig. 5: Halo mass function. Same figure as Fig. 4 for varying magnetic field strengths with the spectral slope kept constant to $n_B = -2.9$.

halo mass function from a known unperturbed one. This will be used in Sec. 4.3.2 to compare the predicted number of Milky Way satellites to the observed ones.

4.2. Zoom-in simulations: physical properties

From each zoom-in simulation, we first extracted the halo corresponding to the reference halo in the unperturbed model. Then, based on the positions and particle IDs, we extracted the analogue of the same halo from the simulations in the perturbed models. For each extracted galaxy, we computed the following quantities defined inside one virial radius R_{200} ¹: the V-band total stellar luminosity L_V , the stellar mass M_\star , the virial mass M_{200} ,

¹ While multiple dark sub-haloes are usually found within R_{200} at $z=0$, the stellar component remain very compact (< 1 kpc). We checked that extracting quantities in a smaller region limited to the size of stellar component does not impact our results.

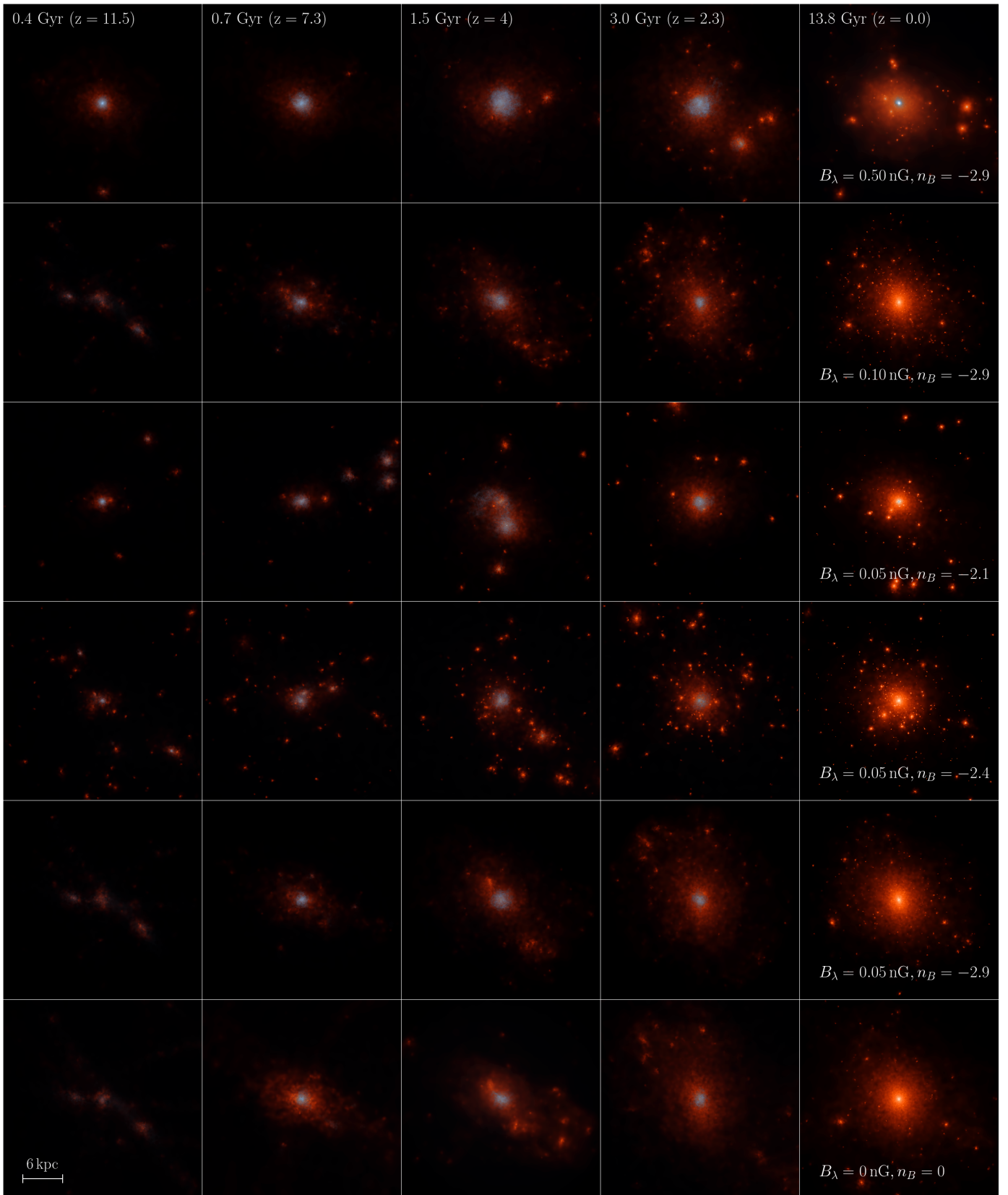


Fig. 6: Time evolution of halo h070 from $z = 11$ to $z = 0$ for different magnetically perturbed models. The unperturbed model is shown at the bottom for comparison. In all images stars are shown in white, the gas is displayed in blue, and the dark matter in orange. Each box is 20 comoving kpc on a side.

the stellar LOS velocity dispersion σ_{LOS} , and the mode of the stellar metallicity distribution function $[\text{Fe}/\text{H}]$. The detail of the procedures used to obtain those quantities is strictly similar to

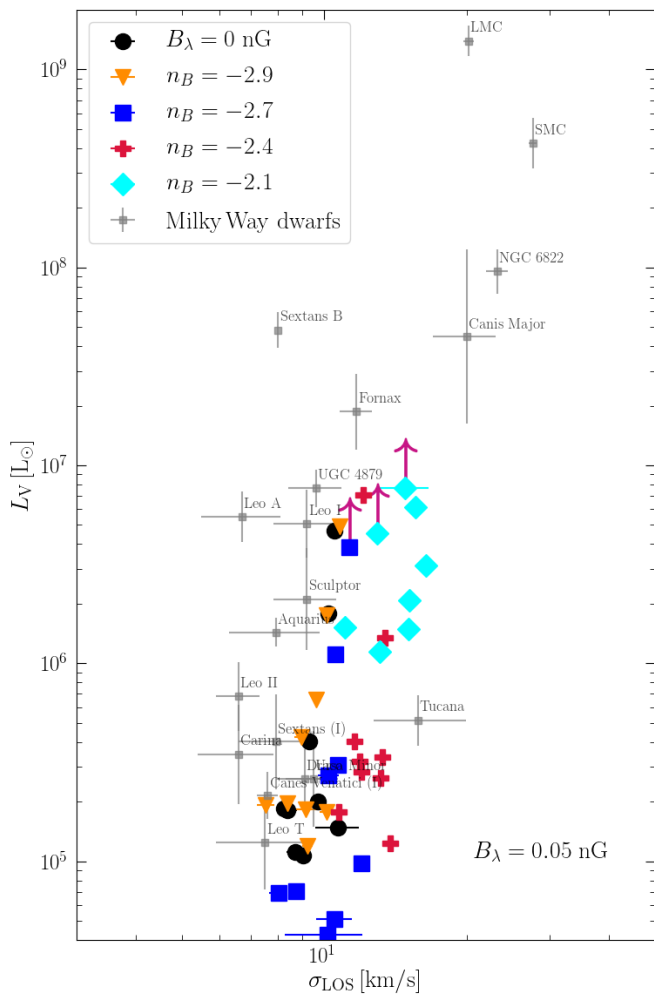


Fig. 7: V-band Luminosity as a function of line-of-sight velocity dispersion in each model galaxy compared to the observational data of Milky Way satellites in black squares (see Sect. 4.2.1 for references). The purple arrows indicate models that did not reach $z = 0$ and are expected to have a slightly brighter luminosity.

the ones used in Revaz & Jablonka (2018). We reported those properties in Tab. A.1.

Figure 6 displays the time evolution of halo h070 for five different magnetically perturbed models ($B_0.50n2.9$, $B0.10n2.9$, $B0.05n2.1$, $B0.05n2.9$), from $z = 11.5$ down to $z = 0$. They are compared to the unperturbed case. Table A.1 together with Fig. 6 reveal the effect of PMFs which can be seen as a sequence along the position and amplitude of the bump in the power spectrum.

In strongly perturbed models with high amplitude B_λ , or high spectral index n_B , i.e., $B0.50n2.9$, $B0.20n2.9$, $B0.05n2.1$, the bump of the power spectrum peaks at mass ranges comparable to the mass scale of dwarf galaxies (10^7 to $10^9 M_\odot$). Those halos start clumping, accreting gas and forming stars earlier. A deep potential well is quickly generated, that prevents the gas reservoir to be evaporated due to the UV-background. Contrary to the unperturbed case where the star formation history is quenched during the epoch of reionization, in the presence of PMFs, the star formation is extended over longer periods, up to Gyrs in the extreme cases, see Fig. 13 and Fig. 14, leading to more massive

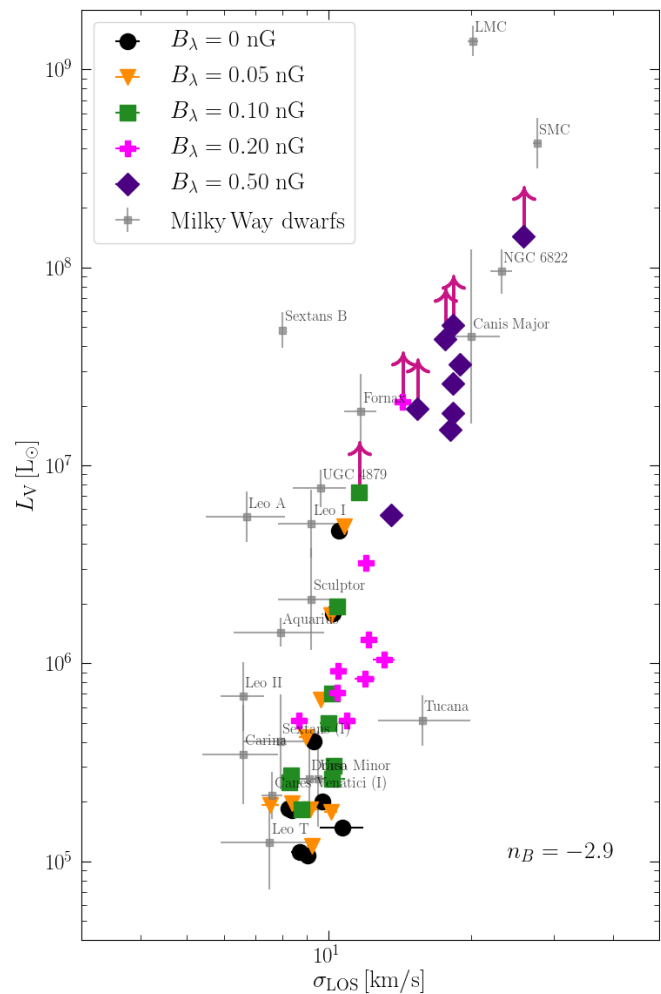


Fig. 8: V-band Luminosity as a function of line-of-sight velocity dispersion. Same figure as Fig. 7 but for models with constant spectral slope and varying magnetic field strengths B_λ .

and brighter galaxies at $z = 0$ with a younger stellar population. Not only the luminosity, but also the dynamics of the systems are affected, e.g., the central LOS velocity dispersion is remarkably larger than its unperturbed analogue, see Fig. 7 and Fig. 8. In extreme cases like $B0.50n2.9$ for more massive haloes h050, h070, h061, h141 the star formation is so intense that it leads to a crash of the code. However, before the crash as we will see further, those models are already too bright and too metallic to be compatible with observed dwarfs.

In weaker PMF models, namely $B0.05n2.9$, $B0.05n2.7$, as the magnetically-induced bump of the power spectrum is in a mass range much below the mass scale of dwarf galaxies ($\lesssim 10^6 M_\odot$) and the amplitude of the bump is not significant, there are no noticeable changes in their built-up history and therefore in their properties. The small differences we see in Tab. A.1 are easily explained by stochasticity. For example, the star formation history is slightly expanded. Indeed, those faint systems are very sensitive to any perturbations.

With a bump at a mass of about $10^7 M_\odot$, models $B0.05n2.4$ and $B0.10n2.9$ are intermediate cases. While their luminosity

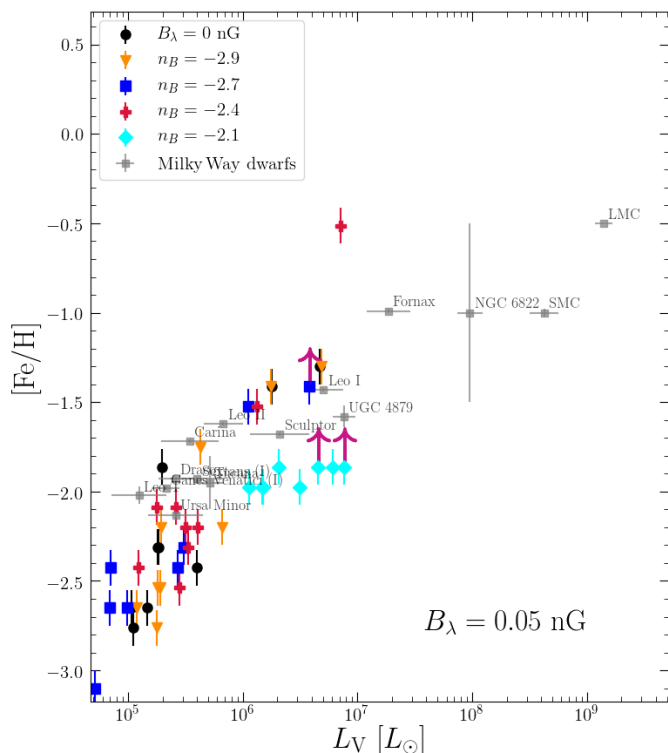


Fig. 9: Mean metallicity vs. stellar V-band Luminosity. Each object corresponds to one model galaxy for which $[\text{Fe}/\text{H}]$ is computed as the median of the galaxy stellar metallicity distribution function. Milky Way satellites are identified with black squares (see Sect. 4.2.1 for references). The purple arrows indicate models that did not reach $z = 0$ and are expected to have a slightly higher metallicity.

and metallicity are weakly affected, a noticeable difference appears in the number of subhalos orbiting each dwarf at $z = 0$, as seen in Fig. 6. The increased number of those dark halos could be an excellent marker of the existence of weak PMFs. Unfortunately, nowadays, they are out of reach from observations, as their effect on the observed properties of dwarfs is negligible and they are not massive enough to be detected through gravitational lensing with current detection limits of about $10^9 M_\odot$ (Vegetti et al. 2010). New forthcoming facilities like the Square Kilometer Array (SKA) will allow the detection of dark substructures with masses as low as $10^6 - 10^7 M_\odot$ through their perturbation on gravitational arcs (McKean et al. 2015).

4.2.1. Zoom-in simulations: scaling relations

Figure 7 and 8 show the galaxy V-band luminosity L_V , as a function of the LOS velocity dispersion σ_{LOS} , while Fig. 9 and 10 show their metallicity (traced by $[\text{Fe}/\text{H}]$) vs. L_V . As comparison to the list of galaxies provided in the compilation of Local Group galaxies by McConnachie (2012), the sample we used essentially restricted to the satellites brighter than $10^5 L_\odot$. For the $[\text{Fe}/\text{H}]$ vs. L_V relation, we used only galaxies that benefit from medium resolution spectroscopy with metallicity derived either from spectral synthesis or Calcium triplet (CaT) calibration. In Revaz & Jablonka (2018), we showed that dwarfs emerging from a classical ΛCDM Universe (i.e., unperturbed model in this work) nicely follow those relations over four orders of

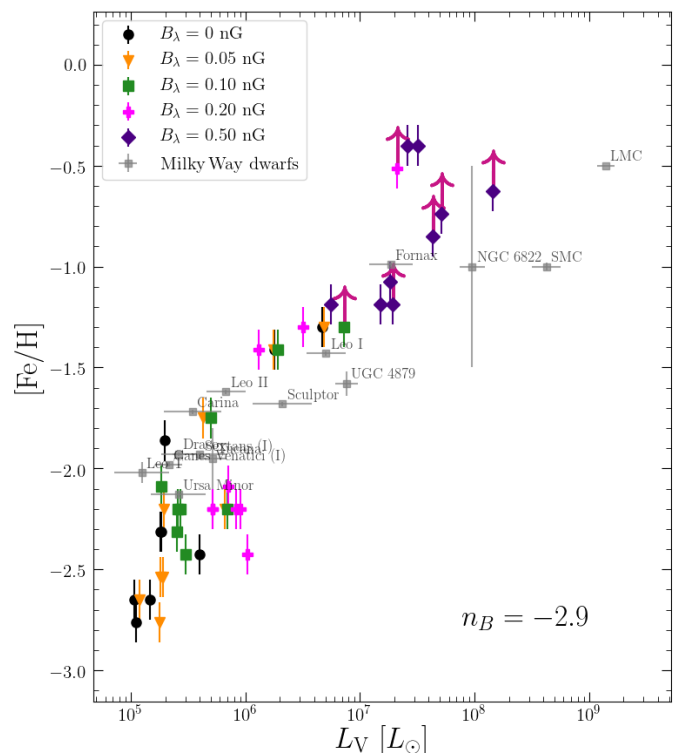


Fig. 10: Mean metallicity vs. stellar V-band Luminosity. Same figure as Fig. 9 but for models with constant n_B and varying magnetic field strengths B_λ .

magnitude from 10^5 to $10^9 L_\odot$. This allows us now to study the impact of PMFs.

The weakly or intermediate perturbed models ($B0.05n2.9$, $B0.05n2.7$, $B0.05n2.4$ and $B0.10n2.9$) still stay on the scaling relations. It is worth noting that model $B0.05n2.7$ suffers from a clear decrease in the luminosity (blue squares). In this model, due to the presence of the bump in the power spectrum at a mass of $\sim 10^6 M_\odot$, many small subhalos are formed. Contrary to more perturbed models they are not massive enough to form stars. This decrease in the luminosity is however not sufficient to rule out this model. The dwarfs emerging from intermediate case $B0.05n2.4$ with their velocity dispersion being increased, fall slightly off the relation. This increase is due to the presence of a larger number of small satellite halos that dynamically heat the stellar component.

The picture becomes however much more different with stronger PMFs. All dwarfs simulated in models $B0.05n2.1$ and $B0.50n2.9$, exhibit star formation histories longer than 2 Gyr, Fig. 13 and Fig. 14. They subsequently become brighter but also denser, with strongly increased velocity dispersion. In the extreme case of model $B0.50n2.9$, while galaxies are still following the L_V vs. σ_{LOS} relation, they produce such a strong quantity of metals that they lie above observed metallicity-luminosity relation, Fig. 10.

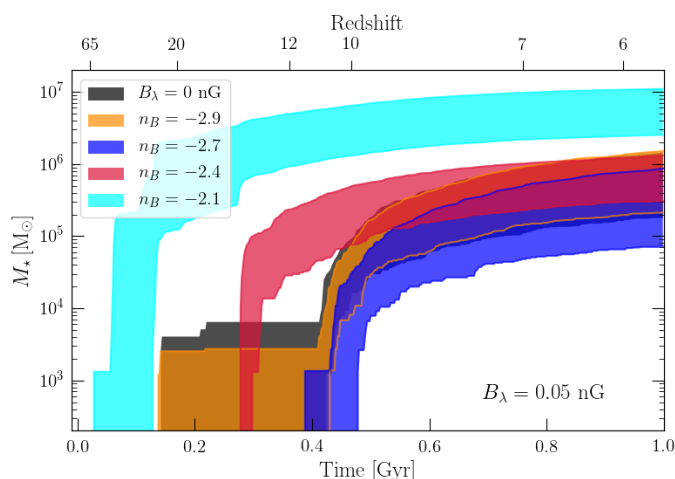


Fig. 11: The cumulative stellar mass in the first Gyr for different models with varying magnetic indices $n_B = -2.9$ to -2.1 . The amplitude of the magnetic field is kept constant at $B_\lambda = 0.05$ nG. Shaded area covers all nine halos simulated in various models.

4.2.2. Luminosity vs. halo mass

As strongly magnetically perturbed models lead to an increase in the star formation rate, we expect the number of stars formed for a given halo mass to be modified. While not directly observed, the stellar mass to halo mass relation is important in particular to predict the number of visible satellites around the Milky Way (See Sec. 4.3.2).

To compute this relation, we extracted all halos found in the refined region of zoom-in simulations, at $z = 0$. We kept only halos containing at least ten stars and polluted by less than five percent of the boundary particles, i.e., particles coming from a region with a lower resolution. For each PMF model, we can then plot the stellar mass content of each halo as a function of its total mass, taken as M_{200} . The results is shown in Fig. 15 and 16. We computed for every model an area delimited by the mean plus/minus one standard deviation of the distribution of galaxy stellar mass within each mass bins. In both figures, the grey area corresponds to the unperturbed model. For the latter, to increase the statistics, we used all dwarfs obtained from the sample of [Revaz & Jablonka \(2018\)](#).

Models $B_{0.05}n_{2.9}$, $B_{0.10}n_{2.9}$, $B_{0.05}n_{2.7}$, and $B_{0.05}n_{2.4}$ display a stellar mass vs. halo mass relation which lie within the bounded area of the unperturbed case.

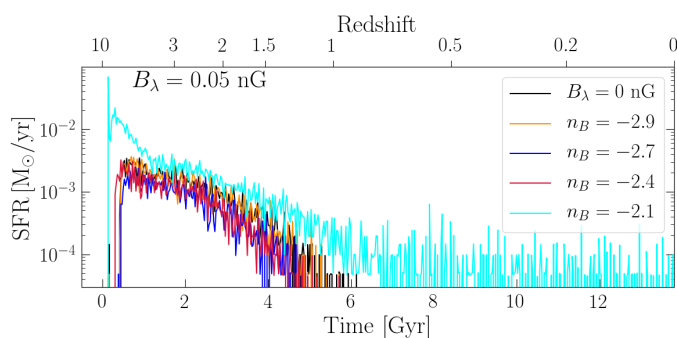


Fig. 13: The star formation rate of halo **h070** for different models with varying magnetic indices $n_B = -2.9$ to -2.1 . The amplitude of the magnetic field is kept constant at $B_\lambda = 0.05$ nG.

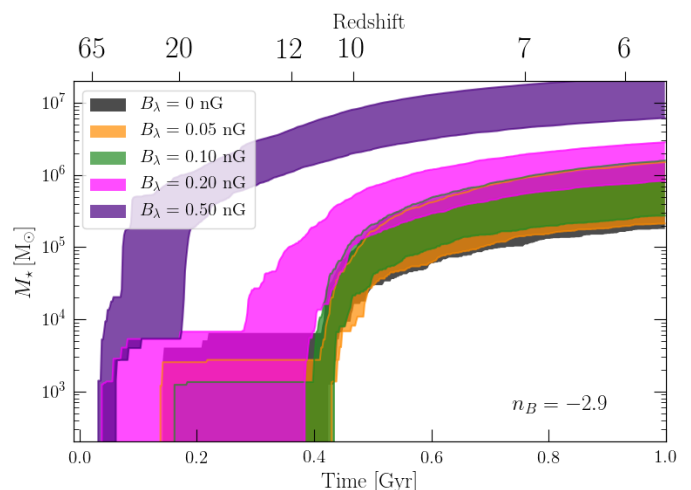


Fig. 12: The cumulative stellar mass in the first Gyr. Same figure as Fig. 11 but for a constant magnetic index $n_B = -2.9$ and a variety of magnetic amplitudes, from $B_\lambda = 0.05$ to $B_\lambda = 0.5$ nG.

Model $B_{0.20}n_{2.9}$ globally lies slightly above. However, the two strongly perturbed models, $B_{0.50}n_{2.9}$ and $B_{0.05}n_{2.1}$ are clearly above. Both produce a much larger quantity of stars, up to one dex, for a given halo mass.

4.3. Cosmic star formation density and the reionization history of the Universe

One striking impact of a strong PMF is to speed-up the formation of dark halos at the dwarf galaxy scale, where the matter power spectrum is amplified (bumps in Fig. 1 and 2). This induces an earlier onset of star formation. This effect is qualitatively seen in Fig. 6 where at $z = 11.5$, a dwarf is clearly formed in models $B_{0.50}n_{2.9}$, $B_{0.05}n_{2.1}$, and $B_{0.05}n_{2.4}$ while the gas has not finished to collapse in the other ones yet.

To estimate this effect quantitatively, Fig. 11 and 12 show the cumulative mass of stars formed during the first Gyr. For each model the upper (resp. the lower) edge of the coloured area corresponds to the cumulative mass of the dwarf which forms the larger (resp. smaller) quantity of stars. For models $B_{0.50}n_{2.9}$ and $B_{0.20}n_{2.9}$ the onset of star formation starts before $z = 50$ while for model $B_{0.05}n_{2.1}$ it starts before $z = 25$, contrary to the unperturbed model in which all dwarfs form stars after

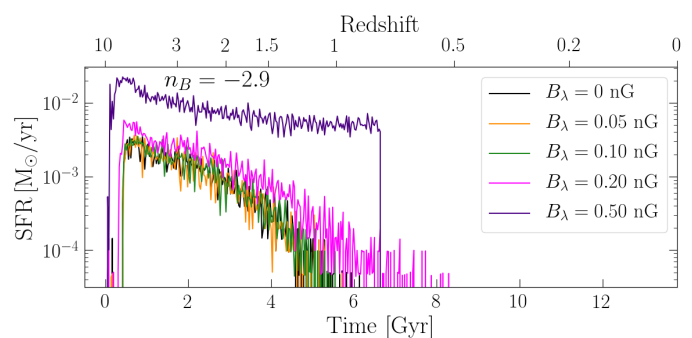


Fig. 14: The star formation rate. Same figure as Fig. 13 but for a constant magnetic index $n_B = -2.9$ and a variety of magnetic amplitudes, from $B_\lambda = 0.05$ to $B_\lambda = 0.5$ nG.

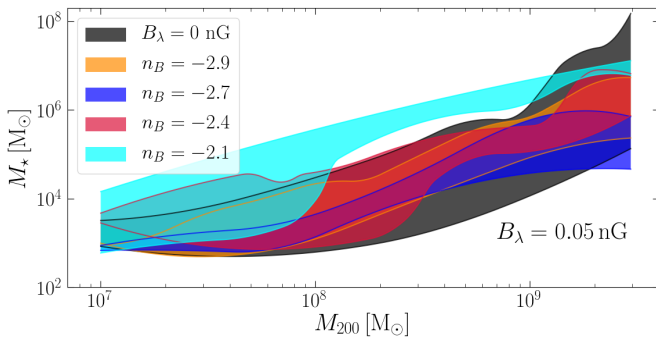


Fig. 15: The stellar mass vs. halo mass relation for different models with a variety of magnetic amplitude B_λ and a constant slope index $n_B = -2.9$.

$z = 25$. In addition, the mean star formation rate is much stronger for models $B_0.50n_{2.9}$ and $B_0.05n_{2.1}$ than the unperturbed model.

With such an early onset of star formation as well as enhancement of the star formation rate, these models will impact the reionization history of the Universe, i.e., the way the globally neutral inter galactic medium (IGM) becomes slowly ionized after being impacted by energetic UV photons generated by young and massive stars. The transition from a neutral IGM to an ionized one is now well constrained by different observations (see [Fan et al. 2006a](#), for a review): the Ly- α absorption by the IGM (the Gunn-Peterson effect) of high redshift quasars ([Fan et al. 2006b](#); [Schroeder et al. 2013](#); [Davies et al. 2018b,a](#); [Greig et al. 2019](#); [Bañados et al. 2018](#); [Durovičková et al. 2020](#)) or gamma-ray bursts ([Totani et al. 2006](#)), the prevalence, spectral properties or clustering of Ly- α emitting galaxies ([Ouchi et al. 2010](#); [Ono et al. 2012](#); [Schenker et al. 2014](#); [Tilvi et al. 2014](#)), and by cosmic microwave background (CMB) polarization through Thomson scattering ([Spergel et al. 2003](#); [Planck Collaboration et al. 2016a](#)). In the following, we describe the method we used to estimate the evolution of the hydrogen ionized fraction from our simulations.

4.3.1. Evolution of the hydrogen ionized fraction

The time evolution of the ionized fraction of hydrogen Q_{HII} may be estimated using a simple differential equation ([Madau et al. 1999](#); [Springel & Hernquist 2003](#); [Kuhlen & Faucher-Giguère 2012](#); [Stoychev et al. 2019](#)):

$$\dot{Q}_{\text{HII}} = \frac{\dot{n}_{\text{ion}}}{\bar{n}_{\text{H}}} - \frac{Q_{\text{HII}}}{t_{\text{rec}}}. \quad (13)$$

The first term on the right hand side describes the ionization source, through the number of ionizing photons while the second one, the sink term, is due to radiative cooling, leading to hydrogen recombination. Further, \dot{n}_{ion} is the global production rate of ionizing photons per unit volume, produced by young and massive stars. It is directly proportional to the cosmic star formation density ρ_{SFR} :

$$\dot{n}_{\text{ion}} = \rho_{\text{SFR}} f_{\text{esc}} \chi_{\text{ion}}, \quad (14)$$

where f_{esc} represents the fraction of ionizing photons that escape star forming regions and χ_{ion} the ionizing photon production efficiency for a typical stellar population per unit time and per unit star formation rate. Moreover, \bar{n}_{H} is the mean comoving hydrogen number density defined through the baryonic fraction Ω_{b} ,

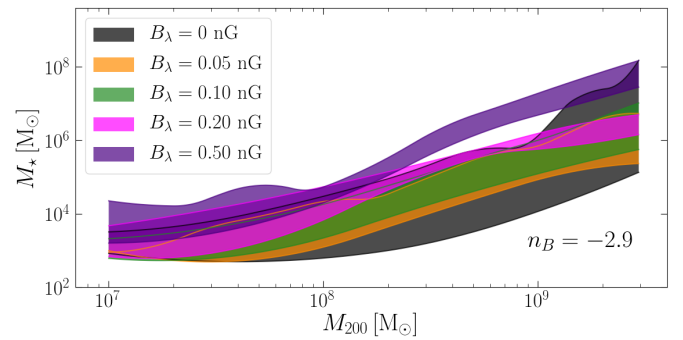


Fig. 16: The stellar mass vs. halo mass relation. Same figure as Fig. 15 but for models with constant $B_\lambda = 0.05$ nG and different slope indexes n_B .

critical density ρ_{c} , hydrogen mass fraction X and hydrogen atom mass m_{H} :

$$\bar{n}_{\text{H}} = \Omega_{\text{b}} X \rho_{\text{c}} / m_{\text{H}}. \quad (15)$$

The source term is due to the radiative recombination of protons with electrons described by the rate of change of the ionized hydrogen proper density n_{HII} :

$$\frac{d}{dt} n_{\text{HII}} = -n_{\text{e}} n_{\text{p}} \alpha_{\text{HII}}(T), \quad (16)$$

where $\alpha_{\text{HII}}(T)$ is the temperature dependent recombination rate coefficient (see [Ferland et al. 1992](#), for tabulated values). Defining X and Y to be the mass fraction of hydrogen and helium respectively, and η the helium ionization degree (0, 1 or 2), we can replace the proper number density of electron n_{e} by $n_{\text{H}} (Q_{\text{HII}} + \eta \frac{Y}{4X})$ as well as the proper number density of proton n_{p} by $n_{\text{H}} Q_{\text{HII}}$. The recombination time t_{rec} of Eq. 13 is then:

$$t_{\text{rec}} = \frac{1}{C_{\text{HII}} (Q_{\text{HII}} + \eta \frac{Y}{4X}) \bar{n}_{\text{H}} (1+z)^3 \alpha_{\text{HII}}(T)} \quad (17)$$

where in the latter equation, we replaced the proper hydrogen density by its comoving expression. An additional clumping factor C_{HII} is added to account for dense regions, self-shielded against ionizing photons that do not contribute to the recombination rate.

For each of our PMF models, we estimated the cosmic star formation density using the following procedure. First, using the Rockstar halo finder, we extracted dark halos from our DMO simulations, at a redshift of 6.3². This provides us with a complete dark halo sample covering $(3.4 \text{ Mpc}/h)^3$ at a redshift near the end of the Epoch of Reionization (EoR). In a second step, using our zoom-in simulations, we extracted at the same redshift, all progenitors of all halos found at $z = 0$ in the refined region³. This provides us with a sample of halos populated by galaxies for which we accurately know the star formation history. In a last step, we attributed to each dark halo (from the dark matter complete sample), a corresponding galaxy, matching their virial

² The choice of this redshift is dictated by a calibration simulation that will be introduced later on. It is sufficient to constrain our models.

³ Halos at $z = 0$ are all halos found in the refined region containing at least ten stellar particles, and being polluted by less than five percent of boundary particles, i.e., particles coming from a region with a lower resolution.

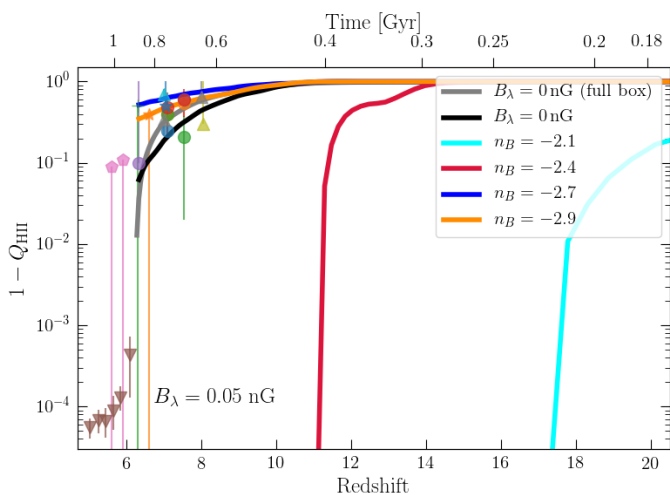


Fig. 17: Time evolution of the neutral hydrogen fraction ($1 - Q_{\text{HII}}$) for models with different slope indexes n_B . The reference simulation (full box) is indicated by the grey curve. The model predictions are compared to observational constraints of the neutral hydrogen fraction from Ly- α absorption of quasars (Fan et al. 2006b) in brown downward triangles, (McGreer et al. 2015) in pink pentagons, (Schroeder et al. 2013) in purple, (Davies et al. 2018b,a) in red, (Greig et al. 2017, 2019) in green, (Bañados et al. 2018) in orange, and (Durovčíková et al. 2020) in blue circles, or gamma-ray bursts (Totani et al. 2006) in green cross and by Ly- α emitting galaxies (Ouchi et al. 2010) in orange star, (Ono et al. 2012) in cyan, (Schenker et al. 2014) in gray, and (Tilvi et al. 2014) in yellow triangles.

mass. This provides us with an estimate of the star formation in the full box and subsequently with the cosmic star formation density. The main difficulty of the method is to correct for the incompleteness of the galaxy samples extracted from the zoom-in simulations. Indeed, these samples are lacking the most luminous objects. This does not limit our analysis as i) more massive and luminous systems are rare and do not dominate the ionizing photons production and ii) including them will lead to a slightly earlier reionization, worsening the situation.

To circumvent this difficulty, we used a simulation run with the same code and parameters (including the full baryonic physics), which used the same initial perturbation field covering the same cosmological volume, but with a homogeneous resolution corresponding to the one of the refined region in the zoom-in simulations. This simulation allowed us to derive a reliable star formation history up to a redshift of 6.3, where it stopped, due to computational expenses. We then calibrated the star formation density derived from our unperturbed zoom-in simulation samples to the full box with a homogeneous resolution. We found a correction factor of 3 to be sufficient to recover the complete star formation history up to $z = 6.3$. We then applied this factor to the star formation density of all others models.

The evolution of the neutral hydrogen fraction $1 - Q_{\text{HII}}$ is then obtained from Eq. 13. Setting $X = 0.76$, $Y = 0.24$, $\eta = 1$ (Faucher-Giguère et al. 2008), $C_{\text{HII}} = 3$ (Kaurov & Gnedin 2015), $\chi_{\text{ion}} = 10^{53}$ photons $(M_{\odot}/\text{yr})^{-1} \text{s}^{-1}$ (Stoychev et al. 2019) and using a fiducial IGM temperature of $2 \cdot 10^4$ K (Hui & Haiman 2003), data are nicely fitted by our unperturbed full box model, if the escape fraction is set to 12%. Keeping this same parameters

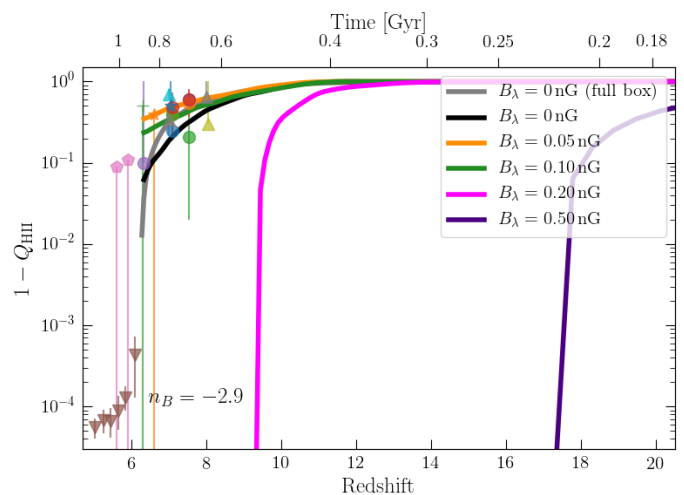


Fig. 18: Time evolution of the neutral hydrogen fraction. Same figure as Fig. 17 but for models with varying magnetic field strengths $B_{\lambda} = 0.05$ to 0.50 nG.

for all models, the evolution of the neutral hydrogen fraction $1 - Q_{\text{HII}}$ is displayed in Fig. 17 and 18.

Due to a strongly enhanced star formation rates, the subsequently large amount of ionizing photons produced by models $B_{\lambda} = 0.05 \text{ nG}$, $B_{\lambda} = 0.10 \text{ nG}$, $B_{\lambda} = 0.20 \text{ nG}$ and $B_{\lambda} = 0.50 \text{ nG}$ lead to a total reionization of the universe at $z < 9$. This is in total disagreement with observational constraints suggesting a reionization starting around $z = 10$ and ending at about $z = 6$ (Bolton & Haehnelt 2007; Loeb & Haiman 1997; Fan et al. 2000; Hu et al. 1999). The other models are in much better agreement. We must emphasize here that our goal was not to precisely reproduce the observations. This requires a much more precise approach, by, for example self-consistently computing the radiative transfer of photons through the ISM and IGM. Our goal was rather to demonstrate that models with important magnetic field perturbation are far off the constraints by a comfortable margin as it is the case here.

In our approach, the growth of structures as well as the star formation histories of dwarfs are self-consistently followed. Our results corroborate results from (Pandey et al. 2015), who estimated the Universe reionization using a semi-analytical estimation of the dark matter collapsed fraction, directly sensitive to matter power spectrum. They found that models with $B_{\lambda} > 0.358, 0.120, 0.059$ nG with respectively $n_B = -2.95, -2.9, -2.85$ are ruled out from existing constraints. Our approach also rules out models with $B_{\lambda} \geq 0.05$ nG and $n_B \geq -2.4$.

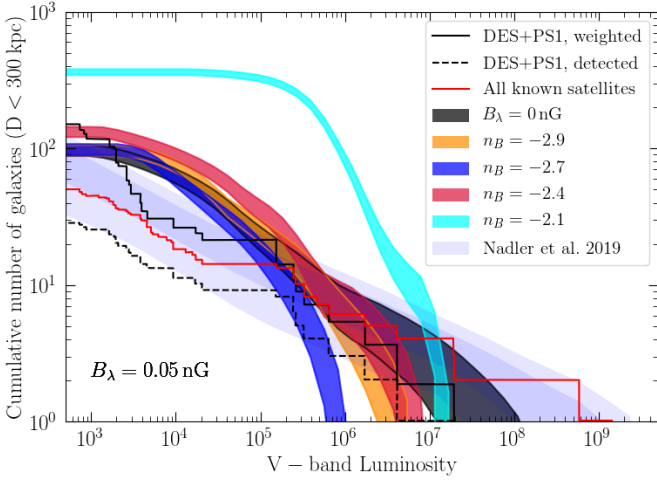


Fig. 19: Predicted cumulative number of satellites brighter than a given luminosity, within 300 kpc around the Milky Way, for models with different slope indexes n_B . For each model, the shaded area corresponds to the mean of thousand realizations of dark matter halos plus or minus one standard deviation. Our predictions are compared to the known satellites shown by the red curve. The dashed black line shows detected satellites in Dark Energy Survey (DES) and Pan-STARRS1 (PS1) as presented in [Drlica-Wagner et al. \(2019\)](#). The solid black line shows the same data but volume corrected, assuming satellites are distributed isotropically. The bluish dashed regions show predictions from cosmological simulations combined with semi-analytical prescriptions ([Nadler et al. 2019](#))

4.3.2. The number of satellites in the Local Group

In Section 4.1 we demonstrated how PMFs may lead to the formation of a larger number of small mass dark halos. This increase may potentially impact the number of observed luminous satellites around the Milky Way. In this section, we aim at estimating the number of expected observed dwarf galaxies brighter than a given luminosity inside 300 kpc and compare it with observations. For this purpose, we combined the halo mass functions obtained in Sec. 4.1 with the luminosity-halo mass relations of the zoom-in hydro-dynamical simulations of Sec. 4.2.2.

Assuming the halo mass function in the unperturbed model follows a power law (Eq. 11), we can obtain an analytical relation of the cumulative abundance of halos $N(> M)$ by multiplying Eq. 11 by the magnetically induced perturbation (Eq. 12) and integrate over the halo mass:

$$N(> M) = -\frac{a}{b+1} M_h^{b+1} + C \left[1 - \operatorname{erf} \left(\frac{\log_{10}(M) - (b+1)s^2 \ln(10) + u}{\sqrt{2}s} \right) \right], \quad (18)$$

Here, erf is the standard error function and the constant C is given by:

$$C = \frac{1}{\sqrt{2}} \sqrt{\pi} a (c-1) s \ln(10) \cdot \exp \left(\frac{(b+1) \ln(10) ((b+1)s^2 \ln(10) + 2u)}{2} \right). \quad (19)$$

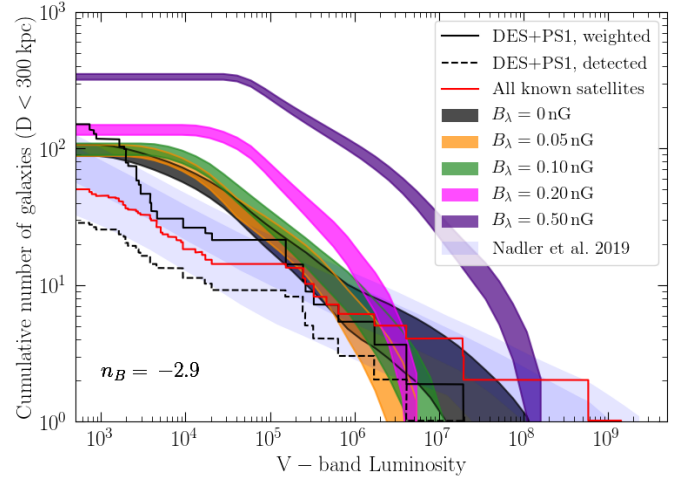


Fig. 20: Predicted cumulative number of satellites brighter than a given luminosity, within 300 kpc around the Milky Way. Same figure as Fig. 19 but for models with varying magnetic field strengths $B_\lambda = 0.05$ to 0.50 nG.

With this notation, the unperturbed case corresponds to $C = 0$.

To reproduce a realistic halo mass function of the Local Group, which includes the perturbative effects of both Milky Way and Andromeda galaxy, we used the cumulative number of dark matter halos inside 300 kpc predicted by the APOSTLE simulations ([Sawala et al. 2017](#)).

The corresponding mass function is obtained by a power law with a slope $b = -1.915$ taken by averaging the slopes of the four different radius bins given in Tab. 2 of [Sawala et al. \(2017\)](#). The amplitude $a = 1.86 \cdot 10^9$ guarantees the existence of 800 dark halos with masses larger than $10^7 M_\odot$ inside 300 kpc. This unperturbed cumulative halo distribution is then perturbed using Eq. 18. Note that for a perturbed halo distribution, the total number of halos with masses larger than $10^7 M_\odot$ increases (up to about 4300 for model $B0.05n2.1$), owing to the bump of the power spectrum that moves masses from smaller to larger scales. Inverting numerically Eq. 18, for each of our models, we randomly generated thousand realizations of dark matter halos using a Monte Carlo approach. Relying on the halo mass vs. luminosity relations (Fig. 15 and 16), we then assigned to each halo a stellar luminosity randomly chosen in the corresponding range showed by the shaded area. Having obtained a luminosity for each halo, we computed the cumulative number of satellites brighter than a given luminosity. Results are shown in Fig. 19 and 20.

Except for models $B0.05n2.1$, $B0.50n2.9$ and $B0.20n2.9$, all models predict twice too many satellites for a luminosity larger than $10^4 L_\odot$ where observed satellites show an intriguing dearth. On the contrary, models $B0.05n2.1$, $B0.50n2.9$ and $B0.20n2.9$ are clearly above the observations, predicting the existence of respectively 16, 12 and 4 times more satellites brighter

than $10^5 L_{\odot}$, compared to what is actually observed. This overabundance results from the combined effect of a larger number of dark halos expected in the mass $10^7 - 10^8 M_{\odot}$ (Fig. 4 and 5) and slightly brighter galaxies populating a given halo mass (Fig. 15 and 16).

We finally note that models with magnetic fields seems to under-predict the number of dwarfs brighter than $10^6 L_{\odot}$. This is only the result of our incomplete sample which lacks bright dwarfs. Indeed, the dark area corresponding to the unperturbed case has been obtained using the total sample of [Revaz & Jablonka \(2018\)](#) which includes dwarfs up to $5 \cdot 10^8 L_{\odot}$. In this case, an excellent match is obtained with observed dwarfs.

The flattening of the curve below $10^3 L_{\odot}$ is the result of the UV-background heating that evaporates gas in the smallest halos and prevents any star formation onset as well as due to our resolution limit.

5. Conclusion

We study the impact of primordial magnetic fields (PMFs) on the formation and evolution of dwarf galaxies through the modification of the Λ CDM matter power spectrum at the recombination era. Depending on the strength and the spectral index of the magnetic field, each PMF model affects the matter power spectrum in a different mass range. We examine a variety of PMF models by either changing the amplitude ($B_{\lambda} = 0.05, 0.10, 0.20, 0.50$ nG) or the slope ($n_B = -2.9, -2.7, -2.4, -2.1$) of the magnetic power spectrum, keeping the other parameters constant.

We first run a set of DMO simulations covering a $(3.4 \text{ Mpc}/h)^3$ box with a resolution of 2×512^3 particles. In a second part, we re-simulate a set of nine halos extracted from the same volume, from redshift $z = 200$ to $z = 0$, using a zoom-in technique and including a full treatment of baryons with the stellar mass resolution of $1024 M_{\odot} h^{-1}$. Our sample of halos in the unperturbed case, give birth to dwarf spheroidals with seven of them having a quenched star formation history and two, an extended one. Our results are summarized as follows:

1. To quantify the contribution of PMFs in the total matter power spectrum, we compute the halo mass function for all our DMO simulations. The ratio of perturbed to unperturbed mass function is well fitted by a simple Gaussian function. We show that increasing the magnetic amplitude B_{λ} , or the slope n_B , increases the number of halos around the maximum of the Gaussian function, up to a factor of 7 in the most extreme cases.

2. We extract the observable properties of each galaxy at redshift $z = 0$, including, the LOS velocity dispersion σ_{LOS} , the peak metallicity, and the total V-band luminosity L_V , to compare them with well observed scaling relations, such as the luminosity vs. velocity dispersion and metallicity vs. luminosity. Strongly perturbed models, with a high amplitude ($B_{\lambda} = 0.5$ nG, $n_B = -2.9$) or a steep spectral index ($n_B = -2.1$, $B_{\lambda} = 0.05$ nG) have more power in the mass range of dwarf galaxies, 10^7 to $10^9 M_{\odot}$. Consequently, in these models, galaxies form more stars and experience an extended star formation history, leading to brighter and more metal rich systems, incompatible with the observed Local Group scaling relations. On the contrary, the observed properties of the weakly perturbed models are not sensitively modified.

3. We show that strong magnetic models speed up the structure formation with an impact on the reionization of the Universe. We estimate the fraction of hydrogen ionized in the first Gyr of the Universe history and demonstrate that earlier onset of star formation as well as the higher rate of forming stars in these models, induces a large amount of ionizing photons, enough to

reionize the universe at redshifts higher than $z = 9$, incompatible with the observational constraints for the EoR.

4. By combining the abundance of dark matter halos obtained from DMO simulations with the luminosity-halo mass function, we derive the number of luminous satellites expected around the Milky Way and show that with high magnetic amplitude or spectral index not only the number of small dark matter halos in mass ranges between 10^7 and $10^8 M_{\odot}$ is raised, but also the stellar mass content for a given halo mass is increased, resulting in an overabundance of satellites brighter than $10^5 L_{\odot}$, contradicting with observations in the Local Group.

We conclude that galaxies simulated in weakly perturbed models resemble all physical properties of their counterparts in the unperturbed model. However, stronger models such as, $B_{\lambda} = 0.05$ nG, with $n_B = -2.4$ or $n_B = -2.1$, and $B_{\lambda} = 0.20$ nG, or $B_{\lambda} = 0.5$ nG, with $n_B = -2.9$ may be ruled out due to the aforementioned reasoning. Our results are consistent with cosmological observables, namely, CMB observations, weak gravitational lensing, Lyman- α data, etc., that constrain the amplitude and the spectral index of the magnetic field power spectrum ([Caprini et al. 2004](#); [Lewis 2004](#); [Kahniashvili et al. 2010](#); [Pandey & Sethi 2012](#); [Trivedi et al. 2012](#); [Shaw & Lewis 2012](#); [Pandey & Sethi 2013](#)). We show that even smaller perturbed models can have a detectable impact on the structure formation.

In this study we considered the contribution of PMFs in the Λ CDM matter power spectrum in mass scales comparable to dwarf galaxies. Regarding the possible direct impact of magnetic fields intrinsic to galaxies, in the proto-stellar scales there are different procedures involved in boosting the star formation rate namely by the angular momentum loss due to the magnetic braking ([Mouschovias & Paleologou 1980](#); [Ferreira et al. 2000](#)), or in contrary suppressing the star formation due to the magnetic pressure ([Burkhart et al. 2009](#); [Molina et al. 2012](#); [Mocz et al. 2017](#); [Sharda et al. 2020](#)). Though, the net effect is still an open question (See [Krumholz & Federrath \(2019\)](#) for a recent review). It is certainly worth studying whether the modification to the star formation history due to the above procedures dominate over the impact of PMFs during the formation of the first structures. To answer that including the full magneto-hydrodynamics (MHD) treatment in our simulations is required. However it is too computationally expensive at this moment. We let this improvement for future studies.

Acknowledgements. We would like to thank Loïc Hausammann, Mladen Ivkovic, and Florian Cabot for very useful discussions. We gratefully acknowledge financial support by Swiss government scholarship FCS. J.S. acknowledges the funding from the European Unions Horizon 2020 research and innovation program under the Marie Skłodowska-Curie Grant No. 665667 and the support by the Swiss National Science Foundation under Grant No. 185863. K.E.K. acknowledges financial support by the Spanish Science Ministry grant PGC2018-094626-B-C22. We acknowledge the support by the International Space Science Institute (ISSI), Bern, Switzerland, for supporting and funding the international team “First stars in dwarf galaxies”. This work was supported by the Swiss Federal Institute of Technology in Lausanne (EPFL) through the use of the facilities of its Scientific IT and Application Support Center (SCITAS). The simulations presented here were run on the Deneb clusters. The data reduction and galaxy maps have been performed using the parallelized Python pNbody package (<http://lastro.epfl.ch/projects/pNbody/>).

References

- Adshead, P., Giblin, John T., J., Scully, T. R., & Sfakianakis, E. I. 2016, *J. Cosmology Astropart. Phys.*, 2016, 039
- Atek, H., Richard, J., Jauzac, M., et al. 2015, *ApJ*, 814, 69
- Aubert, D. & Teyssier, R. 2010, *ApJ*, 724, 244
- Bañados, E., Venemans, B. P., Mazzucchelli, C., et al. 2018, *Nature*, 553, 473
- Banerjee, R. & Jedamzik, K. 2004, *Phys. Rev. D*, 70, 123003
- Beck, R. 2001, *Space Sci. Rev.*, 99, 243

- Beck, R. 2015, *A&A Rev.*, 24, 4
- Beck, R. & Wielebinski, R. 2013, *Magnetic Fields in Galaxies*, ed. T. D. Oswalt & G. Gilmore, Vol. 5, 641
- Behroozi, P. S., Wechsler, R. H., & Wu, H.-Y. 2013, *ApJ*, 762, 109
- Bernet, M. L., Miniati, F., Lilly, S. J., Kronberg, P. P., & Dessauges-Zavadsky, M. 2008, *Nature*, 454, 302
- Bertone, S., Vogt, C., & EnBlin, T. 2006, *MNRAS*, 370, 319
- Bolton, J. S. & Haehnelt, M. G. 2007, *MNRAS*, 382, 325
- Bouwens, R. J., Illingworth, G. D., Oesch, P. A., et al. 2015, *ApJ*, 811, 140
- Boyersky, A., Fröhlich, J., & Ruchayskiy, O. 2012, *Phys. Rev. Lett.*, 108, 031301
- Boylan-Kolchin, M., Bullock, J. S., & Kaplinghat, M. 2011, *MNRAS*, 415, L40
- Boylan-Kolchin, M., Bullock, J. S., & Kaplinghat, M. 2012, *MNRAS*, 422, 1203
- Brandenburg, A., Kahniashvili, T., Mandal, S., et al. 2017a, *Phys. Rev. D*, 96, 123528
- Brandenburg, A., Schober, J., Rogachevskii, I., et al. 2017b, *ApJ*, 845, L21
- Bullock, J. S. & Boylan-Kolchin, M. 2017, *ARA&A*, 55, 343
- Burkhart, B., Falceta-Gonçalves, D., Kowal, G., & Lazarian, A. 2009, *ApJ*, 693, 250
- Caprini, C., Durrer, R., & Kahniashvili, T. 2004, *Phys. Rev. D*, 69, 063006
- Chan, J. H. H., Schive, H.-Y., Woo, T.-P., & Chiueh, T. 2018, *MNRAS*, 478, 2686
- Chan, T. K., Kereš, D., Oñorbe, J., et al. 2015, *MNRAS*, 454, 2981
- Choudhury, T. R., Ferrara, A., & Gallerani, S. 2008, *MNRAS*, 385, L58
- Clarke, T. E., Kronberg, P. P., & Böhringer, H. 2001, *ApJ*, 547, L111
- Davies, F. B., Hennawi, J. F., Bañados, E., et al. 2018a, *ApJ*, 864, 142
- Davies, F. B., Hennawi, J. F., Bañados, E., et al. 2018b, *ApJ*, 864, 143
- Dodelson, S. 2003, *Modern cosmology* (Elsevier)
- Domcke, V., von Harling, B., Morgante, E., & Mukaida, K. 2019, *J. Cosmology Astropart. Phys.*, 2019, 032
- Drlica-Wagner, A., Bechtol, K., Mau, S., et al. 2019, *arXiv e-prints*, arXiv:1912.03302
- Durrer, F. & Dalla Vecchia, C. 2012, *MNRAS*, 419, 465
- Durovčíková, D., Katz, H., Bosman, S. E. I., et al. 2020, *MNRAS*[arXiv:1912.01050]
- Durrer, R. & Neronov, A. 2013, *A&A Rev.*, 21, 62
- Eisenstein, D. J. & Hu, W. 1998, *ApJ*, 496, 605
- Fan, X., Carilli, C. L., & Keating, B. 2006a, *ARA&A*, 44, 415
- Fan, X., Strauss, M. A., Becker, R. H., et al. 2006b, *AJ*, 132, 117
- Fan, X., White, R. L., Davis, M., et al. 2000, *AJ*, 120, 1167
- Faucher-Giguère, C.-A., Lidz, A., Hernquist, L., & Zaldarriaga, M. 2008, *ApJ*, 688, 85
- Ferland, G. J., Peterson, B. M., Horne, K., Welsh, W. F., & Nahar, S. N. 1992, *ApJ*, 387, 95
- Ferland, G. J., Porter, R. L., van Hoof, P. A. M., et al. 2013, *Rev. Mexicana Astron. Astrofis.*, 49, 137
- Ferreira, J., Pelletier, G., & Appl, S. 2000, *Monthly Notices of the Royal Astronomical Society*, 312, 387
- Fitts, A., Boylan-Kolchin, M., Bozek, B., et al. 2019, *MNRAS*, 490, 962
- Fitts, A., Boylan-Kolchin, M., Elbert, O. D., et al. 2017, *MNRAS*, 471, 3547
- Fletcher, A., Beck, R., Shukurov, A., Berkhuijsen, E. M., & Horellou, C. 2011, *MNRAS*, 412, 2396
- Flores, R. A. & Primack, J. R. 1994, *ApJ*, 427, L1
- Fujita, T. & Durrer, R. 2019, *J. Cosmology Astropart. Phys.*, 2019, 008
- Furlanetto, S. R. & Loeb, A. 2001, *ApJ*, 556, 619
- Giovannini, M. & Shaposhnikov, M. 2000, *Phys. Rev. D*, 62, 103512
- Gopal, R. & Sethi, S. K. 2003, *Journal of Astrophysics and Astronomy*, 24, 51
- Governato, F., Weisz, D., Pontzen, A., et al. 2015, *MNRAS*, 448, 792
- Govoni, F. & Feretti, L. 2004, *International Journal of Modern Physics D*, 13, 1549
- Grasso, D. & Rubinstein, H. R. 2001, *Phys. Rep.*, 348, 163
- Greig, B., Mesinger, A., & Bañados, E. 2019, *MNRAS*, 484, 5094
- Greig, B., Mesinger, A., Haiman, Z., & Simcoe, R. A. 2017, *MNRAS*, 466, 4239
- Hahn, O. & Abel, T. 2011, *MNRAS*, 415, 2101
- Han, J. L. 2017, *ARA&A*, 55, 111
- Hanayama, H., Takahashi, K., Kotake, K., et al. 2005, *ApJ*, 633, 941
- Harvey, D., Revaz, Y., Robertson, A., & Hausammann, L. 2018, *MNRAS*, 481, L89
- Hausammann, L., Revaz, Y., & Jablonka, P. 2019, *A&A*, 624, A11
- Hogan, C. J. 1983, *Physics Letters B*, 133, 172
- Hopkins, P. F. 2013, *Pressure-Entropy SPH: Pressure-entropy smooth-particle hydrodynamics*
- Hopkins, P. F., Quataert, E., & Murray, N. 2011, *MNRAS*, 417, 950
- Hu, E. M., McMahon, R. G., & Cowie, L. L. 1999, *ApJ*, 522, L9
- Hui, L. & Haiman, Z. 2003, *ApJ*, 596, 9
- Ichiki, K. & Takahashi, K. 2006, *Astronomical Herald*, 99, 568
- Jedamzik, K., Katalinić, V., & Olinto, A. V. 1998, *Phys. Rev. D*, 57, 3264
- Jedamzik, K., Katalinić, V., & Olinto, A. V. 2000, *Phys. Rev. Lett.*, 85, 700
- Jedamzik, K. & Pogosian, L. 2020 [arXiv:2004.09487]
- Jedamzik, K. & Saveliev, A. 2019, *Phys. Rev. Lett.*, 123, 021301
- Kahniashvili, T., Brandenburg, A., Kosowsky, A., Mandal, S., & Roper Pol, A. 2020, in *IAU General Assembly*, 295–298
- Kahniashvili, T., Tevzadze, A. G., Brandenburg, A., & Neronov, A. 2013, *Phys. Rev. D*, 87, 083007
- Kahniashvili, T., Tevzadze, A. G., Sethi, S. K., Pandey, K., & Ratra, B. 2010, *Phys. Rev. D*, 82, 083005
- Kandus, A., Kunze, K. E., & Tsagas, C. G. 2011, *Phys. Rep.*, 505, 1
- Katz, N. 1992, *ApJ*, 391, 502
- Katz, N., Weinberg, D. H., & Hernquist, L. 1996, *ApJS*, 105, 19
- Kaurov, A. A. & Gnedin, N. Y. 2015, *ApJ*, 810, 154
- Kim, E.-J., Olinto, A. V., & Rosner, R. 1996, *ApJ*, 468, 28
- Klypin, A., Kravtsov, A. V., Valenzuela, O., & Prada, F. 1999, *ApJ*, 522, 82
- Knebe, A., Wagner, C., Knollmann, S., Diekershoff, T., & Krause, F. 2009, *ApJ*, 698, 266
- Kobayashi, C., Tsujimoto, T., & Nomoto, K. 2000, *ApJ*, 539, 26
- Kolb, E. W. & Turner, M. S. 1990, *S&T*, 80, 381
- Krumholz, M. R. & Federrath, C. 2019, *Frontiers in Astronomy and Space Sciences*, 6, 7
- Kuhlen, M. & Faucher-Giguère, C.-A. 2012, *MNRAS*, 423, 862
- Kunze, K. E. & Komatsu, E. 2014, *JCAP*, 01, 009
- Lewis, A. 2004, *Phys. Rev. D*, 70, 043011
- Loeb, A. & Haiman, Z. 1997, *ApJ*, 490, 571
- Lovell, M. R., Eke, V., Frenk, C. S., et al. 2012, *MNRAS*, 420, 2318
- Madau, P., Haardt, F., & Rees, M. J. 1999, *ApJ*, 514, 648
- Mao, S. A., Carilli, C., Gaensler, B. M., et al. 2017, *Nature Astronomy*, 1, 621
- Martin, J. & Yokoyama, J. 2008, *J. Cosmology Astropart. Phys.*, 2008, 025
- Mateo, M. L. 1998, *ARA&A*, 36, 435
- McBride, J. & Heiles, C. 2013, *ApJ*, 763, 8
- McConnachie, A. W. 2012, *AJ*, 144, 4
- McGreer, I. D., Mesinger, A., & D’Odorico, V. 2015, *MNRAS*, 447, 499
- McKean, J., Jackson, N., Vegetti, S., et al. 2015, in *Advancing Astrophysics with the Square Kilometre Array (ASKA14)*, 84
- Mocz, P., Burkhart, B., Hernquist, L., McKee, C. F., & Springel, V. 2017, *ApJ*, 838, 40
- Molina, F. Z., Glover, S. C. O., Federrath, C., & Klessen, R. S. 2012, *MNRAS*, 423, 2680
- Moore, B. 1994, *Nature*, 370, 629
- Moore, B., Ghigna, S., Governato, F., et al. 1999, *ApJ*, 524, L19
- Mouschovias, T. C. & Paleologou, E. V. 1980, *ApJ*, 237, 877
- Nadler, E. O., Mao, Y.-Y., Green, G. M., & Wechsler, R. H. 2019, *ApJ*, 873, 34
- Nadler, E. O., Mao, Y.-Y., Wechsler, R. H., Garrison-Kimmel, S., & Wetzel, A. 2018, *ApJ*, 859, 129
- Naoz, S. & Narayan, R. 2013, *Phys. Rev. Lett.*, 111, 051303
- Navarro, J. F., Frenk, C. S., & White, S. D. M. 1996, *ApJ*, 462, 563
- Navarro, J. F., Frenk, C. S., & White, S. D. M. 1997, *ApJ*, 490, 493
- Neronov, A. & Vovk, I. 2010, *Science*, 328, 73
- Newton, O., Cautun, M., Jenkins, A., Frenk, C. S., & Helly, J. C. 2018, *MNRAS*, 479, 2853
- Oñorbe, J., Boylan-Kolchin, M., Bullock, J. S., et al. 2015, *MNRAS*, 454, 2092
- Okamoto, T., Eke, V. R., Frenk, C. S., & Jenkins, A. 2005, *MNRAS*, 363, 1299
- Ono, Y., Ouchi, M., Mobasher, B., et al. 2012, *ApJ*, 744, 83
- Ouchi, M., Shimasaku, K., Furusawa, H., et al. 2010, *ApJ*, 723, 869
- Padmanabhan, T. 2002, *Theoretical Astrophysics - Volume 3, Galaxies and Cosmology*, Vol. 3
- Pandey, K. L., Choudhury, T. R., Sethi, S. K., & Ferrara, A. 2015, *MNRAS*, 451, 1692
- Pandey, K. L. & Sethi, S. K. 2012, *ApJ*, 748, 27
- Pandey, K. L. & Sethi, S. K. 2013, *ApJ*, 762, 15
- Paoletti, D., Chluba, J., Finelli, F., & Rubiño-Martín, J. A. 2019, *MNRAS*, 484, 185
- Planck Collaboration, Adam, R., Aghanim, N., et al. 2016a, *A&A*, 596, A108
- Planck Collaboration, Ade, P. A. R., Aghanim, N., et al. 2015, *A&A*, 582, A29
- Planck Collaboration, Ade, P. A. R., Aghanim, N., et al. 2016b, *A&A*, 594, A13
- Pontzen, A. & Governato, F. 2014, *Nature*, 506, 171
- Ratra, B. 1992a, *ApJ*, 391, L1
- Ratra, B. 1992b, *ApJ*, 391, L1
- Read, J. I., Walker, M. G., & Steger, P. 2018, *MNRAS*, 481, 860
- Reiners, A. 2012, *Living Reviews in Solar Physics*, 9, 1
- Revaz, Y., Arnaudon, A., Nichols, M., Bonvin, V., & Jablonka, P. 2016, *A&A*, 588, A21
- Revaz, Y. & Jablonka, P. 2012, *A&A*, 538, A82
- Revaz, Y. & Jablonka, P. 2018, *A&A*, 616, A96
- Robertson, B. E., Ellis, R. S., Furlanetto, S. R., & Dunlop, J. S. 2015, *ApJ*, 802, L19
- Robishaw, T., Quataert, E., & Heiles, C. 2008, *ApJ*, 680, 981
- Rogachevskii, I., Ruchayskiy, O., Boyarsky, A., et al. 2017, *ApJ*, 846, 153
- Ryu, D., Kang, H., Cho, J., & Das, S. 2008, *Science*, 320, 909
- Safarzadeh, M. 2018, *MNRAS*, 479, 315
- Safarzadeh, M. & Loeb, A. 2019, *ApJ*, 877, L27
- Salvadori, S., Tolstoy, E., Ferrara, A., & Zaroubi, S. 2014, *MNRAS*, 437, L26

- Sawala, T., Frenk, C. S., Fattahi, A., et al. 2016, MNRAS, 457, 1931
- Sawala, T., Pihajoki, P., Johansson, P. H., et al. 2017, MNRAS, 467, 4383
- Schenker, M. A., Ellis, R. S., Konidaris, N. P., & Stark, D. P. 2014, ApJ, 795, 20
- Schober, J., Rogachevskii, I., Brandenburg, A., et al. 2018, ApJ, 858, 124
- Schober, J., Schleicher, D. R. G., & Klessen, R. S. 2013, A&A, 560, A87
- Schroeder, J., Mesinger, A., & Haiman, Z. 2013, MNRAS, 428, 3058
- Sethi, S. K. & Subramanian, K. 2005, MNRAS, 356, 778
- Sharda, P., Federrath, C., & Krumholz, M. R. 2020, arXiv e-prints, arXiv:2002.11502
- Shaw, J. R. & Lewis, A. 2010, Phys. Rev. D, 81, 043517
- Shaw, J. R. & Lewis, A. 2012, Phys. Rev. D, 86, 043510
- Silk, J. 1968, ApJ, 151, 459
- Simon, J. D. 2019, ARA&A, 57, 375
- Smith, B. D., Bryan, G. L., Glover, S. C. O., et al. 2017, MNRAS, 466, 2217
- Spergel, D. N., Verde, L., Peiris, H. V., et al. 2003, ApJS, 148, 175
- Springel, V. 2005, MNRAS, 364, 1105
- Springel, V. & Hernquist, L. 2003, MNRAS, 339, 312
- Springel, V., Wang, J., Vogelsberger, M., et al. 2008, MNRAS, 391, 1685
- Stevenson, D. J. 2010, Space Sci. Rev., 152, 651
- Stoychev, B. K., Dixon, K. L., Macciò, A. V., Blank, M., & Dutton, A. A. 2019, MNRAS, 489, 487
- Subramanian, K. 2016, Reports on Progress in Physics, 79, 076901
- Subramanian, K. & Barrow, J. D. 1998, Phys. Rev. Lett., 81, 3575
- Tashiro, H., Silk, J., Langer, M., & Sugiyama, N. 2009, MNRAS, 392, 1421
- Tegmark, M. & Zaldarriaga, M. 2002, Phys. Rev. D, 66, 103508
- Tilvi, V., Papovich, C., Finkelstein, S. L., et al. 2014, ApJ, 794, 5
- Tolstoy, E., Hill, V., & Tosi, M. 2009, ARA&A, 47, 371
- Tornatore, L., Borgani, S., Dolag, K., & Matteucci, F. 2007, MNRAS, 382, 1050
- Totani, T., Kawai, N., Kosugi, G., et al. 2006, PASJ, 58, 485
- Trivedi, P., Seshadri, T. R., & Subramanian, K. 2012, Phys. Rev. Lett., 108, 231301
- Tsujiimoto, T., Nomoto, K., Yoshii, Y., et al. 1995, MNRAS, 277, 945
- Turner, M. S. & Widrow, L. M. 1988a, Phys. Rev. D, 37, 2743
- Turner, M. S. & Widrow, L. M. 1988b, Phys. Rev. D, 37, 2743
- Vachaspati, T. 1991, Physics Letters B, 265, 258
- Vegetti, S., Koopmans, L. V. E., Bolton, A., Treu, T., & Gavazzi, R. 2010, MNRAS, 408, 1969
- Verbeke, R., Papastergis, E., Ponomareva, A. A., Rathi, S., & De Rijcke, S. 2017, A&A, 607, A13
- Vogelsberger, M., Zavala, J., Simpson, C., & Jenkins, A. 2014, MNRAS, 444, 3684
- Vogt, C. & EnBlin, T. A. 2005, A&A, 434, 67
- Wagstaff, J. M. & Banerjee, R. 2015, Phys. Rev. D, 92, 123004
- Wasserman, I. 1978a, ApJ, 224, 337
- Wasserman, I. M. 1978b, PhD thesis, HARVARD UNIVERSITY.
- Wetzel, A. R., Hopkins, P. F., Kim, J.-h., et al. 2016, ApJ, 827, L23
- Widrow, L. M. 2002, Reviews of Modern Physics, 74, 775
- Wiersma, R. P. C., Schaye, J., Theuns, T., Dalla Vecchia, C., & Tornatore, L. 2009, MNRAS, 399, 574
- Wise, J. H., Demchenko, V. G., Halicek, M. T., et al. 2014, MNRAS, 442, 2560
- Zucca, A., Li, Y., & Pogosian, L. 2017, Phys. Rev. D, 95, 063506

Appendix A: Physical Properties of model galaxies

Table A.1: Physical properties of all model galaxies. For each galaxy we computed the V-band total stellar luminosity L_V , the stellar mass M_* , the virial mass M_{200} , the virial radius R_{200} , the stellar line-of-sight velocity dispersion σ_{LOS} , and the mode of the stellar metallicity distribution function [Fe/H], all defined inside one virial radius. In the first row, different PMF models are shown at a variety of magnetic spectral indices between -2.9 to -2.1 for constant $B_\lambda = 0.05$, and in the second row for a constant spectral index at $n_B = -2.9$ and magnetic field strengths between $B_\lambda = 0.05 - 0.50$ nG.

model ID	B_λ [rmnG]	n_B -	L_V [$10^6 L_\odot$]	M_* [$10^6 M_\odot$]	M_{200} [$10^9 M_\odot$]	R_{200} kpc	σ_{LOS} [kms $^{-1}$]	[Fe/H] dex	Redshift ⁴ / Time - / [Gyr]
h050									
B0.00n0.0	0.00	0.0	4.66	10.01	2.66	33.14	10.52	-1.30	0.00 / 13.8
B0.05n2.9	0.05	-2.9	4.90	10.47	2.67	33.18	10.80	-1.30	0.00 / 13.8
B0.05n2.7		-2.7	3.84	7.60	2.63	32.98	11.30	-1.41	0.06 / 13.0
B0.05n2.4		-2.4	7.10	12.29	2.46	32.25	12.09	-0.51	0.00 / 13.8
B0.05n2.1		-2.1	-	-	-	-	-	-	24.6 / 0.13
B0.10n2.9	0.10	-2.9	7.33	13.76	2.62	32.94	11.61	-1.30	0.04 / 13.3
B0.20n2.9	0.20		20.99	31.93	2.51	32.49	14.35	-0.51	0.11 / 12.3
B0.50n2.9	0.50		143.40	147.52	3.51	36.33	25.83	-0.62	0.62 / 7.8
h070									
B0.00n0.0	0.00	0.0	1.78	5.13	1.80	29.08	10.20	-1.41	0.00 / 13.8
B0.05n2.9	0.05	-2.9	1.76	5.05	1.78	28.99	10.11	-1.41	0.00 / 13.8
B0.05n2.7		-2.7	1.11	3.13	1.81	29.13	10.57	-1.52	0.00 / 13.8
B0.05n2.4		-2.4	1.34	3.84	1.93	29.74	13.46	-1.52	0.00 / 13.8
B0.05n2.1		-2.1	6.13	17.16	1.61	28.02	15.61	-1.86	0.00 / 13.8
B0.10n2.9	0.10	-2.9	1.93	5.52	1.79	29.00	10.44	-1.41	0.00 / 13.8
B0.20n2.9	0.20		3.21	9.34	1.84	29.32	12.00	-1.30	0.00 / 13.8
B0.50n2.9	0.50		51.22	53.89	2.38	31.90	18.28	-0.74	0.83 / 6.6
h061									
B0.00n0.0	0.00	0.0	0.20	0.50	1.95	29.85	9.72	-1.86	0.00 / 13.8
B0.05n2.9	0.05	-2.9	0.18	0.43	1.96	29.91	10.10	-2.76	0.00 / 13.8
B0.05n2.7		-2.7	0.04	0.09	1.98	30.00	10.16	-3.89	0.00 / 13.8
B0.05n2.4		-2.4	0.28	0.75	1.79	29.02	12.00	-2.54	0.00 / 13.8
B0.05n2.1		-2.1	7.68	13.37	1.80	29.05	14.81	-1.86	0.75 / 7.0
B0.10n2.9	0.10	-2.9	0.30	0.74	1.94	29.82	10.25	-2.42	0.00 / 13.8
B0.20n2.9	0.20		1.05	2.75	2.02	30.23	13.10	-2.42	0.00 / 13.8
B0.50n2.9	0.50		43.60	48.94	2.59	32.82	17.66	-0.85	0.69 / 7.4
h141									
B0.00n0.0	0.00	0.0	0.18	0.49	0.78	21.98	8.22	-2.31	0.00 / 13.8
B0.05n2.9	0.05	-2.9	0.20	0.52	0.78	21.97	8.36	-2.20	0.00 / 13.8
B0.05n2.7		-2.7	0.07	0.18	0.78	22.05	8.73	-2.42	0.00 / 13.8
B0.05n2.4		-2.4	0.26	0.72	0.87	22.78	13.17	-2.09	0.00 / 13.8
B0.05n2.1		-2.1	4.52	8.39	0.84	22.53	12.94	-1.86	0.67 / 7.5
B0.10n2.9	0.10	-2.9	0.27	0.71	0.81	22.31	8.33	-2.20	0.00 / 13.8
B0.20n2.9	0.20		0.71	1.95	0.79	22.10	10.43	-2.09	0.00 / 13.8
B0.50n2.9	0.50		19.26	20.80	1.08	24.49	15.42	-1.19	1.13 / 5.4
h111									
B0.00n0.0	0.00	0.0	0.15	0.36	1.06	24.40	10.71	-2.65	0.00 / 13.8
B0.05n2.9	0.05	-2.9	0.18	0.45	1.05	24.26	9.13	-2.54	0.00 / 13.8
B0.05n2.7		-2.7	0.10	0.23	1.07	24.43	11.99	-2.65	0.00 / 13.8
B0.05n2.4		-2.4	0.34	0.91	0.93	23.29	13.26	-2.31	0.00 / 13.8
B0.05n2.1		-2.1	3.13	8.98	0.88	22.92	16.41	-1.98	0.00 / 13.8
B0.10n2.9	0.10	-2.9	0.26	0.64	1.06	24.38	10.15	-2.20	0.00 / 13.8
B0.20n2.9	0.20		0.83	2.21	1.19	25.32	11.94	-2.20	0.00 / 13.8
B0.50n2.9	0.50		32.33	65.88	1.95	29.86	18.98	-0.40	0.00 / 13.8
h122									
B0.00n0.0	0.00	0.0	0.11	0.26	0.93	23.37	9.02	-2.65	0.00 / 13.8
B0.05n2.9	0.05	-2.9	0.12	0.30	0.96	23.61	9.22	-2.65	0.00 / 13.8
B0.05n2.7		-2.7	0.05	0.12	0.89	22.98	10.53	-3.10	0.00 / 13.8
B0.05n2.4		-2.4	0.12	0.32	0.86	22.77	13.81	-2.42	0.00 / 13.8

Table A.1: continued.

model ID	B_λ [nG]	n_B -	L_V [$10^6 L_\odot$]	M_\star [$10^6 M_\odot$]	M_{200} [$10^9 M_\odot$]	R_{200} kpc	σ_{LOS} [kms^{-1}]	[Fe/H] dex	Redshift / Time - / [Gyr]
B0.05n2.1		-2.1	1.48	4.13	0.84	22.56	15.05	-1.98	0.00 / 13.8
B0.10n2.9	0.10	-2.9	0.18	0.46	0.91	23.17	8.77	-2.09	0.00 / 13.8
B0.20n2.9	0.20		0.52	1.36	0.90	23.12	10.92	-2.20	0.00 / 13.8
B0.50n2.9	0.50		25.93	53.81	1.54	27.60	18.33	-0.40	0.00 / 13.8
h159									
B0.00n0.0	0.00	0.0	0.40	1.03	0.68	21.02	9.31	-2.42	0.00 / 13.8
B0.05n2.9	0.05	-2.9	0.43	1.09	0.68	21.05	8.96	-1.75	0.00 / 13.8
B0.05n2.7		-2.7	0.27	0.69	0.67	20.93	10.23	-2.42	0.00 / 13.8
B0.05n2.4		-2.4	0.40	1.10	0.59	20.09	11.59	-2.20	0.00 / 13.8
B0.05n2.1		-2.1	2.08	6.06	0.65	20.73	15.12	-1.86	0.00 / 13.8
B0.10n2.9	0.10	-2.9	0.50	1.29	0.68	21.00	9.98	-1.75	0.00 / 13.8
B0.20n2.9	0.20		0.91	2.49	0.67	20.93	10.49	-2.20	0.00 / 13.8
B0.50n2.9	0.50		15.10	36.82	1.64	28.18	18.10	-1.19	0.00 / 13.8
h168									
B0.00n0.0	0.00	0.0	0.11	0.27	0.54	19.42	8.68	-2.76	0.00 / 13.8
B0.05n2.9	0.05	-2.9	0.66	1.79	2.88	34.01	9.60	-2.20	0.00 / 13.8
B0.05n2.7		-2.7	0.31	0.81	2.70	33.29	10.70	-2.31	0.00 / 13.8
B0.05n2.4		-2.4	0.32	0.88	1.14	24.93	11.90	-2.20	0.00 / 13.8
B0.05n2.1		-2.1	1.51	4.43	0.52	19.18	11.08	-1.98	0.00 / 13.8
B0.10n2.9	0.10	-2.9	0.70	1.92	2.68	33.20	10.15	-2.20	0.00 / 13.8
B0.20n2.9	0.20		1.31	3.67	2.31	31.61	12.15	-1.41	0.00 / 13.8
B0.50n2.9	0.50		18.36	40.09	1.43	26.94	18.34	-1.08	0.00 / 13.8
h177									
B0.00n0.0	0.00	0.0	0.18	0.47	0.52	19.26	8.35	-2.31	0.00 / 13.8
B0.05n2.9	0.05	-2.9	0.19	0.50	0.52	19.22	7.53	-2.54	0.00 / 13.8
B0.05n2.7		-2.7	0.07	0.17	0.51	19.07	8.02	-2.65	0.00 / 13.8
B0.05n2.4		-2.4	0.18	0.49	0.37	17.08	10.72	-2.09	0.00 / 13.8
B0.05n2.1		-2.1	1.14	3.18	0.68	21.06	13.11	-1.98	0.00 / 13.8
B0.10n2.9	0.10	-2.9	0.25	0.65	0.54	19.42	8.27	-2.31	0.00 / 13.8
B0.20n2.9	0.20		0.52	1.40	0.56	19.67	8.64	-2.20	0.00 / 13.8
B0.50n2.9	0.50		5.63	17.27	0.94	23.41	13.54	-1.19	0.00 / 13.8

⁴ halos which did not reach $z = 0$ crashed at redshift specified here. The reason some simulations crashed at $z > 0$ is due the increase in the mass content of more massive halos in strong models which consequently leads to extremely massive galaxies with a very early onset and high rate of star formation.